Article

Tectono-Thermal Evolution and Morphodynamics of the Central Dronning Maud Land Mountains, East Antarctica, Based on New Thermochronological Data

Hallgeir Sirevaag [1,*] **, Anna K. Ksienzyk** [1,†] **, Joachim Jacobs** [1] **, István Dunkl** [2] **and Andreas Läufer** [3]

[1]   Department of Earth Science, University of Bergen, P.O. Box 7803, 5020 Bergen, Norway; Anna.Ksienzyk@ngu.no (A.K.K.); Joachim.Jacobs@uib.no (J.J.)

[2]   Geoscience Centre, University of Göttingen, Goldschmidtstraβe 3, 37077 Göttingen, Germany; Istvan.Dunkl@geo.uni-goettingen.de

[3]   Bundesanstalt für Geowissenschaften u. Rohstoffe, Stilleweg 2, 30655 Hannover, Germany; Andreas.Laeufer@bgr.de

*   Correspondence: Hallgeir.Sirevaag@gmail.com; Tel.: +47-93-28-87-39

†   Present Address: Geological Survey of Norway, P.O. Box 6315 Torgarden, 7491 Trondheim, Norway.

check for updates

Abstract: The lack of preserved Mesozoic–Cenozoic sediments and structures in central Dronning Maud Land has so far limited our understanding of the post-Pan-African evolution of this important part of East Antarctica. In order to investigate the thermal evolution of the basement rocks and place constraints on landscape evolution, we present new low-temperature thermochronological data from 34 samples. Apatite fission track ages range from 280–85 Ma, while single-grain (U-Th)/He ages from apatite and zircon range from 305–15 and 420–340 Ma, respectively. Our preferred thermal history models suggest late Paleozoic–early Mesozoic peneplanation and subsequent burial by 3–6 km of Beacon sediments. The samples experienced no additional burial in the Jurassic, thus the once voluminous continental flood basalts of western Dronning Maud Land did not reach central Dronning Maud Land. Mesozoic–early Cenozoic cooling of the samples was slow. Contrary to western Dronning Maud Land, central Dronning Maud Land lacks a mid-Cretaceous cooling phase. We therefore suggest that the mid-Cretaceous cooling of western Dronning Maud Land should be attributed to the proximity to the collapse of the orogenic plateau at the Panthalassic margin of Gondwana. Cooling rates accelerated considerably with the onset of glaciation at 34 Ma, due to climate deterioration and glacial denudation of up to 2 km.

Keywords: apatite fission track; (U-Th)/He; low-temperature thermochronology; thermal modelling; passive margin; Gondwana rifting

1. Introduction

The Dronning Maud Land Mountains in East Antarctica form an impressive, largely coast-parallel mountain range with a total relief exceeding 5 km, extending for c. 1500 km in length. The highest peaks reach elevations up to c. 3200 m a.s.l., while the deepest incisions are 2 km below sea level. The Dronning Maud Land Mountains originated as a continental margin escarpment following the break-up of Gondwana in Jurassic times. This escarpment is now located c. 200 km inland of the continental margin. Here, we focus on a c. 350 km long section in central Dronning Maud Land from Mühlig-Hofmannfjella in the west to Wohlthatmassivet in the east (Figures 1 and 2). The exposed basement comprises Mesoproterozoic–Early Paleozoic high-grade rocks, documenting a protracted older geodynamic evolution, including the formation and destruction of two supercontinents—Rodinia and Gondwana, e.g., [1,2].
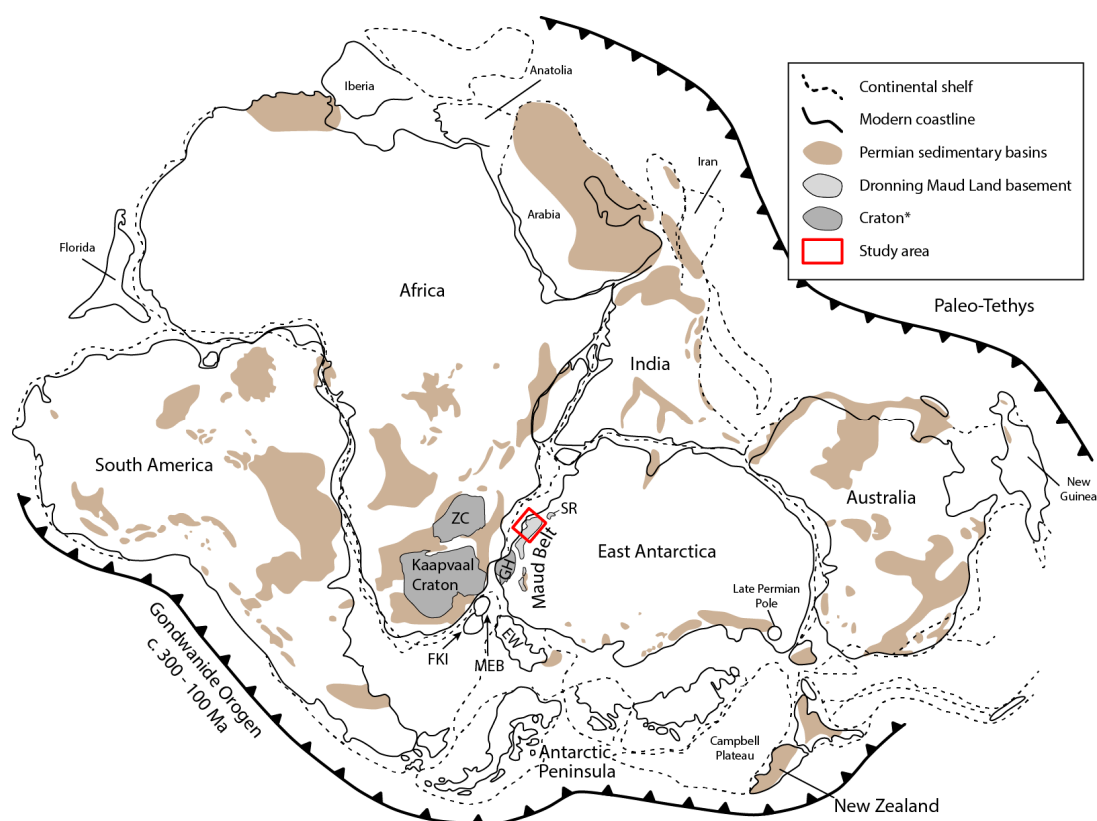
Figure 1. Gondwana reconstruction during Permian times, showing the distribution of Permian sedimentary basins. * Only cratons that were part of the Kalahari Craton are shown. Abbreviations: EW—Ellsworth-Whitmore Mountains crustal blocks; FKI—Falkland Islands; GH—Grunehogna Craton; MEB–Maurice Ewing Bank; SR—Sør-Rondane; ZC—Zimbabwe Craton. Modified after Storey and Kyle [3], König and Jokat [4], Boger [5], Slater et al. [6] and Stone [7].

Applying low-temperature thermochronology on central Dronning Maud Land basement rocks allows us to trace the tectonic and morphodynamic evolution during pre-, syn- and post-break-up times in a region that lacks marker horizons, such as unconformable overlying sedimentary rocks. Previously published thermochronological data from the area are interpreted to reflect long-lasting monotonic cooling of the basement since the last orogeny in Early Paleozoic times [8–10]. Similar datasets from western and eastern Dronning Maud Land have revealed a much more complex thermal evolution of the mountain range, e.g., [11–14], including Late Paleozoic–Early Mesozoic peneplanation and syn-rift reburial, either due to sedimentary basins or by emplacement of Jurassic continental flood basalts. This apparently contrasting long-term tectonic and morphodynamic evolution is puzzling, and has raised several questions: Was the basement in central Dronning Maud Land also exposed to the surface during the Late Paleozoic–Early Mesozoic? Were the central Dronning Maud Land Mountains covered by Jurassic continental flood basalts or Mesozoic sedimentary basins? What did the central Dronning Maud Land Mountains look like at the onset of the glaciation?

In order to trace the evolution of the central Dronning Maud Land Mountains since the Early Paleozoic, we have revisited the area with modern fission track dating and the addition of new apatite and zircon (U-Th)/He analyses (AHe and ZHe, respectively). Meier [8] and Meier et al. [9] still used non-standard etching techniques for their apatite fission track analyses and also used a somewhat unconventional zeta calibration approach. We have therefore re-analyzed many of Meier's samples to bring them up to the standard required for state-of-the-art thermochronological modelling. Additionally, new samples have been added from Schirmacheroasen (Figures 2 and 3). Based on this dataset, we present new thermal history models from 34 samples that shed light on the sedimentation, erosion and exhumation history of the central Dronning Maud Land Mountains.

2. Regional Geology

Central Dronning Maud Land comprises two distinct geological provinces: the Mesoproterozoic Maud Belt and the northwestern part of the Tonian Oceanic Arc Super Terrane (TOAST; [15]). Dronning Maud Land is commonly placed adjacent to SE Africa in Gondwana reconstructions, e.g., [16–24], and hence the Maud Belt is generally interpreted as the southern continuation of the Mesoproterozoic Mozambique and Namaqua-Natal belts, e.g., [1,23,25–28].

In central Dronning Maud Land, the Maud Belt preserves evidence of the assembly of both Rodinia (Grenvillian Orogeny) and Gondwana (Pan-African Orogeny). The basement of the Maud Belt is characterized by initial felsic volcanism at c. 1130 Ma and polyphase granulite-facies metamorphism at c. 1080 Ma, c. 590–550 Ma and c. 530–485 Ma [22,29,30]. The Late Mesoproterozoic metamorphic event is associated with the incorporation of Dronning Maud Land into Rodinia, while the two Late Neoproterozoic–Early Cambrian metamorphic events are related to the collisional phase during Gondwana assembly, resulting in the major East African–Antarctic Orogen (EAAO; e.g., [31]), and the subsequent extensional collapse of this orogen [30], respectively. To the west, the orogenic front of the EAAO is exposed as the 20 km wide, dextral Heimefront Shear Zone in Heimefrontfjella, e.g., [32–34].

In the eastern part of central Dronning Maud Land, three major NE–SW trending lineaments separate the Maud Belt from the Tonian Oceanic Arc Super Terrane ([15,35]; Figures 2 and 3). The Tonian Oceanic Arc Super Terrane is characterized by 1000–900 Ma juvenile basement, similar to the gabbro-trondhjemite-tonalite-granodiorite suite that can be found in the SW-Terrane of the Sør-Rondane Mountains further east. The subsequent evolution of the Tonian Oceanic Arc Super Terrane is similar to that of the Maud Belt in central Dronning Maud Land, including polyphase reworking and granitoid intrusions between c. 630 and c. 490 Ma [15].
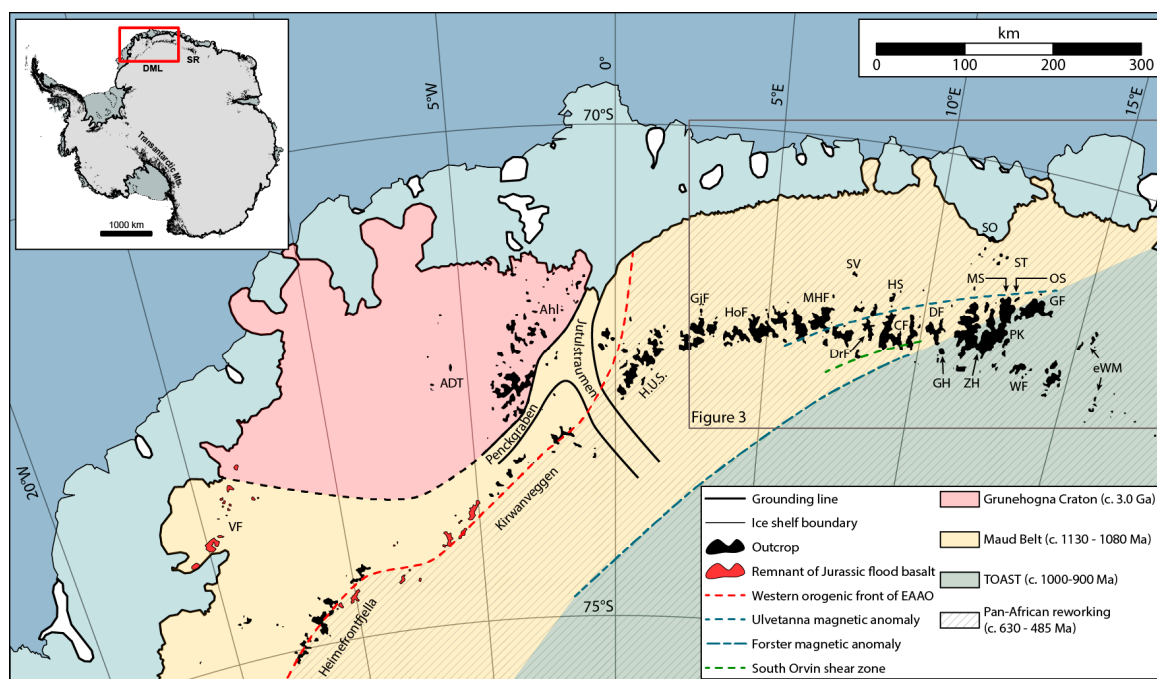

Figure 2. Simplified geological map of western and central Dronning Maud Land. Abbreviations: ADT—Annandagstoppane; Ahl—Ahlmannryggen; CF—Conradfjella; DF—Dallmannfjellet; DrF—Drygalskifjella; eWM—Eastern Wohlthatmassivet; GF—Gruberfjella; GH—Gjeruldsenhøgda; GjF—Gjelsvikfjella; HoF—Hochlinfjellet; HS—Henriksenskjera; H.U.S.—H.U. Sverdrupfjella; MHF—Mühlig-Hofmannfjella; MS—Madsensåta; OS—Oddenskjera; PK—Petermannkjedene; SO—Schirmacheroasen; SR—Sør-Rondane; ST—Starheimtind; SV—Sigurdsvodene; VF—Vestfjella; WF—Weyprechtfjella; ZH—Zwieselhøgda. Lineaments after Jacobs and Lisker [11], Bauer et al. [34] and Jacobs et al. [36].
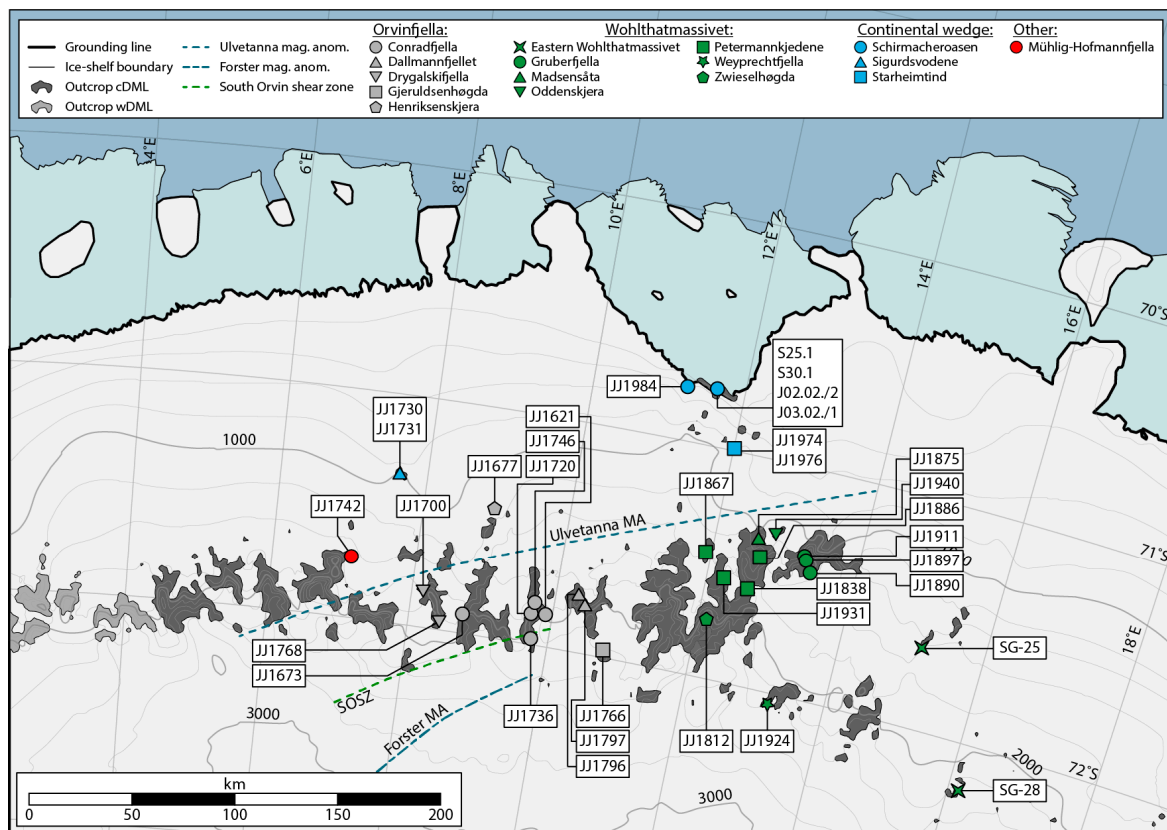
Figure 3. Overview map of sample localities and major lineaments. Lineaments after Jacobs et al. [36].

Post-Pan-African Evolution

The post-Pan-African evolution of Dronning Maud Land is difficult to resolve due to the scarcity of preserved onshore Phanerozoic sediments; in central Dronning Maud Land, no Phanerozoic sedimentary rocks are exposed at all. When Gondwana had formed, two major active continental margin systems evolved on its northern and southern sides (Figure 1). The southern Panthalassic margin evolved into a long-lasting active continental margin that significantly influenced the tectonic evolution of East Antarctica from Paleozoic–Mesozoic times, e.g., [37] and led to the formation of large sedimentary basins (Figure 1). In western Dronning Maud Land, Phanerozoic sediments include only up to c. 160 m of Late Carboniferous–Middle Permian Beacon sediments [38–42]. Within the Transantarctic Mountains, on the other hand, a much more complete sedimentary succession is preserved, comprising up to c. 3 km of Devonian to Triassic siliciclastic Beacon sediments [43–45]. Equivalents of the Beacon sediments are widespread all-over southeastern Africa, along the conjugate margin to Dronning Maud Land, where sediments of the Karoo Supergroup are preserved in cumulative thicknesses of up to c. 12 km (e.g., [46]; Figure 1).

In western Dronning Maud Land and within the Transantarctic Mountains, the Beacon sediments unconformably overlie Mesoproterozoic and Cambrian–Ordovician basement rocks, forming a distinct paleosurface, e.g., [42,45]. Relics of a paleosurface, interpreted to be of similar age, have also been identified at Jutulsessen in Gjelsvikfjella [47]. In Sør-Rondane (eastern Dronning Maud Land), low-relief surfaces have been identified, but their age is still debated. These surfaces are mainly composed of glacially abraded bedrock without any preserved glacial deposits and it has therefore been suggested that they formed during an older glaciation [48,49], making them potentially of the same age as the paleosurfaces further west.

During the early stages of Gondwana fragmentation, large amounts of continental flood basalts associated with the Karoo mantle plume were emplaced at c. 183 Ma [50–54]. Today, these are exposed in thicknesses up to c. 5 km within the Lebombo Monocline in southeastern Africa, whereas they are only preserved in thicknesses up to c. 1 km in Vestfjella and up to c. 400 m within the southwestern Maud Belt in western Dronning Maud Land [51,55–59]. Based on thermochronological data, however, it has been suggested that western Dronning Maud Land was covered by up to 2 km of Jurassic continental flood basalts, extending at least as far east as Hochlinfjellet at c. 4° E [11,14]. Exposures of continental flood basalts have not been reported further east in central Dronning Maud Land, but Jurassic mafic dykes in Petermannkjedene and at Schirmacheroasen have been associated with the Karoo magmatism [60,61].

The initial fragmentation of Gondwana started in Early Jurassic times with the separation of East- and West Gondwana along the Davie Fracture zone and other related transform faults, e.g., [62,63]. Continued rifting eventually led to the Middle Jurassic separation of Antarctica and Africa, resulting in the opening of pull-apart-type basins, such as the western Riiser-Larsen Sea and the Mozambique Basin, e.g., [5,62,63]. The oldest sea floor anomalies within the western Riiser-Larsen Sea have been dated to c. 155 Ma, and thus represent the latest possible age of the onset of the separation [62,64]. The fragmentation continued with the separation of India from both Antarctica and Australia at c. 135 Ma, e.g., [65], the opening of the eastern Riiser-Larsen Sea at c. 124 Ma [62], and the separation of Australia from Antarctica at c. 95 Ma [66]. It has furthermore been suggested that during the Cretaceous, a high orogenic plateau formed along the Panthalassic continental margin. This plateau began to collapse at ca. 105 Ma, leading to the formation of the West Antarctic Rift System, e.g., [67].

The post-rift evolution of Dronning Maud Land has mainly been inferred from offshore data. Seaward-dipping reflectors (Early Jurassic volcanics; [68,69]) overlain by c. 0.7–2.9 km of Cenozoic sediments have been documented between 25° W and 9° E. During ODP (Ocean Drilling Program) leg 113, five sites (sites 689–693) from the Maud Rise, north of central Dronning Maud Land, and on the eastern Weddell Sea margin were drilled [70,71]. These cores comprise uppermost Cretaceous–Cenozoic sediments, providing detailed information of the paleoclimate, including the growth of the East Antarctic ice sheet. Additionally, Quaternary sediments have been drilled at the Riiser-Larsen Ice Shelf, eastern Weddell Sea. These sediments are characterized by detritus from the Jurassic continental flood basalts and subordinate plutonic and/or metamorphic basement rocks [72].

The sediments from the ODP drill sites indicate that Dronning Maud Land was characterized by a temperate–cool subtropical climate during latest Cretaceous times, followed by generally increasing temperatures throughout the Late Paleocene, reaching a climax in Middle Eocene times. These ODP data also indicate a progressively cooler climate later throughout the late Eocene, eventually leading to formation and major growth of the East Antarctic ice sheet in late Eocene–Early Oligocene times [70].

3. Previous Thermochronological Results

Central Dronning Maud Land has been targeted by one quite extensive fission track study in the 1990s [8,9]. It has to be pointed out, however, that Meier [8] and Meier et al. [9] used non-standard etching techniques for their apatite fission track analyses, as well as an unconventional zeta calibration approach. This limits the usefulness of their track lengths measurements for thermochronological modelling, and also their fission track ages should be regarded with some caution. Titanite yielded fission track ages from Late Ordovician to Early Permian times [8], whereas zircon fission track ages are Late Devonian to Middle Triassic [8,9]. Early–Middle Jurassic apatite fission track ages clearly dominate the sample suite, although AFT ages as old as Middle Carboniferous and as young as Late Cretaceous are also present [8,9]. Emmel et al. [10] report the only available (U-Th)/He analyses for central Dronning Maud Land; apatite (U-Th)/He ages from six samples range from Late Carboniferous to mid-Cretaceous. These published datasets from central Dronning Maud Land have been interpreted

to record cooling since the Pan-African Orogeny until the present day, with periods of slow cooling interrupted by several episodes of faster cooling [8–10]. The three main phases of accelerated cooling reported in central Dronning Maud Land have been related to Early Jurassic Gondwana rifting and the evolution of the passive margin [8–10], the opening of the western Riiser-Larsen Sea and the detachment of India from Antarctica during the Late Jurassic, and the mid-Cretaceous accelerated northward drift of India [8,9], respectively.

To the west of our study area, low-temperature thermochronological data have been reported from Ahlmannryggen and Annandagstoppane within the Archean Grunehogna Craton [14], and the Maud Belt between Heimefrontfjella in the southwest and Hochlinfjellet in the northeast [11,12,14,73]. Zircon (U-Th)/He analyses gave Neoproterozoic to Triassic single-grain ages, although most ages are either Permian or Ordovician, indicating that most of the samples had reached upper crustal depths either shortly after the Pan-African Orogeny or during the late Paleozoic peneplanation of western Dronning Maud Land [14].

The apatite fission track ages from western Dronning Maud Land range from Carboniferous to mid-Cretaceous. The dataset is dominated by Cretaceous and Triassic ages, with the oldest ages found at high elevations (such as Kirwanveggen), but the AFT ages also generally increase towards Hochlinfjellet in the east [11,12,14]. The apatite (U-Th)/He analyses yielded a wide range of single-grain ages, spanning from Early Ordovician to Eocene. Late Jurassic to Cretaceous ages are, however, predominant in western Dronning Maud Land [14,73]. Based on the combined apatite fission track and (U-Th)/He dataset, it has been suggested that western Dronning Maud Land was buried under up to 2 km of Jurassic continental flood basalts during Gondwana rifting [11,14]. This was followed by Late Jurassic–Cretaceous cooling related to rifting of East- and West Gondwana, subsequent opening of the South Atlantic, major plate reorganization and enhanced chemical weathering [11,14]. A final phase of Early–Middle Cenozoic cooling is recorded, associated with the onset of the glaciation, either as a result of increased glacial erosion [14], or due to differential exhumation and flexural isostatic rebound due to the load of the developing ice sheet [73].

4. Samples and Analytical Methods

Thirty-four samples from basement rocks of the Pan-African Maud Belt and the Tonian Oceanic Arc Super Terrane in central Dronning Maud Land are included in this study (Table 1). Twenty-eight of the samples have previously been analyzed by Meier [8], while six new samples are also included. The samples come from the mountain crest itself or from its northern side in areas between c. 7° E (Mühlig-Hofmannfjella) and c. 16° E (eastern Wohlthatmassivet) (Figure 3). Most of the samples come from elevations between c. 1000 m a.s.l. and c. 3000 m a.s.l., except for five samples from c. 50–150 m a.s.l. at Schirmacheroasen, close to the coastline. The samples have been selected according to their localities and elevations in order to analyze a representative sample suite from the Dronning Maud Land escarpment. The apatite and zircon concentrates were extracted using standard mineral separation techniques, including a shaking table, followed by magnetic- and heavy-liquid separation.

By combining apatite fission track analyses with apatite and zircon (U-Th)/He analyses, a wide temperature range is covered. The partial annealing zone (PAZ) of the fission track system ranges from c. 60 °C to c. 120 °C, e.g., [74]. The partial retention zones (PRZ) for apatites and zircons with low degrees of metamictization are c. 35–70 °C and c. 150–230 °C, respectively, e.g., [75,76], although more recent studies have proven that radiation damage strongly affects the closure temperatures of the different (U-Th)/He systems [77,78].

Table 1. List of samples used in the present study.

Sample	Lithology	Locality	Province	Coordinates Lat.	Long.	Elev. (m)	Analyses
			Mühlig-Hofmannfjella				
JJ742	Granitic gneiss	Mühlig-Hofmannfjella	Maud Belt	−71.7333	7.1000	1410	AFT AHe
			Orvinfjella				
JJ700	Syenite	Drygalskifjella	Maud Belt	−71.8436	8.1574	1745	AFT AHe
JJ768	Migmatic metavolcanic	Drygalskifjella	Maud Belt	−71.9652	8.4410	2145	AFT AHe
JJ621	Granite	Conradfjella	Maud Belt	−71.8604	9.9019	1785	AHe
JJ673	Gneiss	Conradfjella	Maud Belt	−71.9167	8.7500	1200	AFT AHe
JJ720	Tonalite	Conradfjella	Maud Belt	−71.8667	9.7000	2985	AFT AHe
JJ736	Augen gneiss	Conradfjella	Maud Belt	−71.9744	9.7532	2605	AFT AHe
JJ746	Tonalite/granodiorite	Conradfjella	Maud Belt	−71.8165	9.7276	1590	AFT AHe
JJ766	Syenite	Gjeruldsenhøgda	TOAST	−71.9667	10.7833	2100	AFT AHe
JJ796	Orthogneiss	Dallmannfjellet	Maud Belt	−71.7448	10.3676	1745	AFT AHe
JJ797	Augen gneiss	Dallmannfjellet	Maud Belt	−71.7824	10.4172	1745	AFT AHe
JJ677	Leucogranite	Henriksenskjera	Maud Belt	−71.4352	8.9637	1315	AFT AHe
			Wohlthatmassivet				
JJ812	Gabbro	Zwieselhøgda	TOAST	−71.7441	12.1185	2965	AFT AHe
JJ838	Gneiss	Petermannkjedene	TOAST	−71.5785	12.5861	1260	AFT AHe
JJ867	Granitic gneiss	Petermannkjedene	Maud Belt	−71.4592	11.9171	1410	AFT AHe
JJ886	Augen gneiss	Petermannkjedene	Boundary	−71.4312	12.6599	1125	AFT AHe
JJ931	Granodiorite-dike	Petermannkjedene	Boundary	−71.5554	12.2358	1475	AFT AHe
JJ875	Syenite	Madsensåta	Maud Belt	−71.3500	12.5833	1400	AFT AHe
JJ890	Anorthosite	Gruberfjella	TOAST	−71.4499	13.3777	2800	AFT AHe
JJ897	Anorthosite	Gruberfjella	TOAST	−71.4000	13.2833	2175	AFT AHe
JJ911	Gneiss	Gruberfjella	TOAST	−71.3833	13.2500	1285	AFT AHe
JJ924	Gneiss	Weyprechtfjella	TOAST	−72.0500	13.2167	2685	AFT AHe
JJ940	Biotite-fluorite granite	Oddenskjera	Maud Belt	−71.3233	12.8054	1190	AFT AHe
SG-25*	Metadiorite	E. Wohlthatmassivet	TOAST	−71.6459	15.1205	1795	AHe
SG-28*	Migmatitic gneiss	E. Wohlthatmassivet	TOAST	−72.2001	16.1512	2285	AHe
			Continental wedge				
JJ730	Felsic gneiss	Sigurdsvodene	Maud Belt	−71.3500	7.6167	1035	AFT AHe
JJ731	Hornblende gneiss	Sigurdsvodene	Maud Belt	−71.3500	7.6167	1155	AFT AHe
JJ974	Granodiorite-dike	Starheimtind	Maud Belt	−71.0000	12.0167	1075	AHe
JJ976	Diorite	Starheimtind	Maud Belt	−71.0000	12.0167	1345	AFT AHe
JJ984	Augen gneiss	Schirmacheroasen	Maud Belt	−70.7667	11.2333	50	AFT AHe
S25.1*		Schirmacheroasen	Maud Belt	−70.7502	11.6232	150	AFT AHe
S30.1*		Schirmacheroasen	Maud Belt	−70.7502	11.6232	150	AFT AHe
J02.02/2*	Augen gneiss	Schirmacheroasen	Maud Belt	−70.7502	11.6232	150	ZHe
J03.02/1*	Augen gneiss	Schirmacheroasen	Maud Belt	−70.7502	11.6232	150	ZHe

Table footnote: Samples marked with * represent new samples. The remaining samples have previously been analyzed by Meier [8], but are re-analyzed in this study. Coordinates are approximate outcrop coordinates from maps.

4.1. Apatite Fission Track Analyses

Apatites from 31 samples were analyzed by the fission track technique (AFT), applying the external detector method [79]. The apatite crystals were first mounted in epoxy, then ground and polished to expose an internal crystal surface. The grain mounts were etched in 5 M nitric acid for 20 s at $20 \pm 0.5\,^{\circ}$C in order to reveal the spontaneous fission tracks. External mica detectors were placed on top of the grain mounts, and the sample packages were irradiated at the FRM II research reactor at the Technical University of Munich (Germany), using a thermal neutron flux of 1×10^{16} neutrons/cm^2. The neutron flux was monitored by using the dosimeter glasses IRMM-540R. The mica detectors were then etched for 20 min in 40% hydrofluoric acid at room temperature in order to reveal the induced tracks.

The fission track analyses were conducted on an Olympus BX51 optical microscope equipped with a computer-driven stage and the FT-Stage software [80] at the Department of Earth Science, University of Bergen, Norway. For fission track counting, a magnification of 1250× was used. The AFT central ages were calculated by the TrackKey software [81], applying the zeta calibration approach [82] with a zeta calibration factor of 214 ± 5 (H. Sirevaag).

Etch-pit diameters (Dpar; [83]) and confined track lengths were measured using a magnification of 2000×. As Dpar can be used as a proxy for apatite annealing kinetics, five Dpars were measured for each grain that was counted, and three Dpars were measured for each measured confined track length. Only track-in-tracks (TinTs) were considered for the track length measurements. If possible, 100 TinTs were measured for each sample.

4.2. (U-Th)/He Analyses

(U-Th)/He analyses were conducted on apatite crystals from 33 samples and zircon crystals from two samples. The grains were analyzed at the GÖochron Laboratories, Geoscience Center, University of Göttingen, Germany. The individual grains were carefully evaluated and handpicked under binocular and petrographic microscopes in order to avoid fractures and mineral- and fluid-inclusions as far as possible. The grains were photographed for determining crystal dimensions and then packed individually in platinum capsules. The ^{4}He content was determined by degassing under high vacuum by heating with an infrared diode laser for 2 min. The extracted gas was purified with a SAES Ti–Zr getter at 450 $^{\circ}$C and analyzed with a Hiden triple-filter quadrupole mass spectrometer, equipped with a positive ion-counting detector. During sequential reheating and He measurements, the crystals were checked for complete degassing of He (re-extract).

The platinum capsules were removed after the He analyses in order to measure the U, Th and Sm contents. The apatites were dissolved in a 4% HNO_3 + 0.05% HF acid mixture in Savillex teflon vials, and the zircons were dissolved in a pressurized teflon bomb with a mixture of double-distilled 48% HF and 65% HNO_3. The dissolved crystals were spiked with calibrated ^{230}Th and ^{233}U solutions and analyzed by the isotope dilution method either on a Perkin Elmer Elan DRC II, or by a Thermo iCAP Q ICP-MS, equipped with an APEX micro-flow nebulizer. Alpha-ejection correction (F_T-correction) was applied to the raw (U-Th)/He ages after the procedures described by Farley et al. [84] and Hourigan et al. [85].

The (U-Th)/He dataset was carefully evaluated. Grains with a He re-extract > 5%, total analytical uncertainty > 10%, or grains that were statistical outliers compared to the remaining single-grain analyses in the same sample according to the Grubbs and Dixon tests [86–88] were excluded. Excluded grains are not included in any figures, calculations or thermal models, but are reported together with the remaining dataset in italic.

4.3. Modelling of the Thermal History

The software HeFTy v. 1.9.1 [89] was used for the thermal history modelling. For the AFT data, we applied the annealing model of Ketcham et al. [90], as well as c-axis projection of the confined track lengths according to Ketcham et al. [91]. The radiation damage accumulation and annealing model of Flowers et al. [92] and the model of Guenthner et al. [78] were used for modelling apatite

and zircon (U-Th)/He data, respectively. As most samples include more than one thermochronometer, all thermochronometers in a sample were generally modelled together. In cases where it was not possible to model all (U-Th)/He data and AFT data together, the "problematic" analyses were excluded from the model. "Problematic" analyses have been identified by testing various combinations of AFT data and single-grain AHe analyses and, if necessary, excluding single-grain AHe analyses that are incompatible with the remaining AHe analyses and/or the fission track analyses from the same sample (i.e., prevent the model from finding any cooling paths). The thermochronometers that were used are specified for each model.

During the thermal modelling, 100,000 random paths were tested. In the following sections, we use the best-fit and weighted mean paths of the acceptable (goodness-of-fit ≥ 0.05) and good (goodness-of-fit ≥0.5) paths for comparisons of the models. The goodness-of-fit is calculated by using Kuiper's statistics in HeFTy [89].

In order to model the thermal histories, external *t*–*T* constraints must be applied, based on pre-existing thermochronological and geological evidence. For all thermal models, similar start and end constraints were applied. As a starting constraint, we used biotite ^{40}Ar–^{39}Ar ages of c. 450 Ma from Filchnerfjella (westernmost Orvinfjella) in the westernmost part of our study area [93], recording temperatures of c. 300–350 °C. The present-day surface temperature (−25 °C) is used as the end constraint. We have tested different geological scenarios, which will be discussed in more detail below. Briefly, three sets of models have been run:

(1)   simple cooling with only start and end constraints.
(2)   late Paleozoic peneplanation with subsequent late Paleozoic–early Mesozoic burial beneath sediments. For these models, we inferred the position of the late Paleozoic peneplain by connecting mountain peaks from the escarpment to the hinterland. These peaks define a gently southward sloping surface, which we interpreted as the last remnant of the peneplain. Based on glacial deposits within both the Beacon sediments in Heimefrontfjella and the Karoo Supergroup in south-central Africa, e.g., [42,94,95], we have applied a surface temperature of −10 °C and corrected the temperature for each sample based on their vertical distance to the extrapolated peneplain, assuming a geothermal gradient of 25 °C/km (this has been done for all following steps as well). This approach works well for the main mountain range but not for samples from the coast (e.g., Schirmacheroasen)—they were generally given a lot more freedom during the modelling to account for the uncertainty in their position with regard to the extrapolated peneplain. A second constraint box allows for Permo-Triassic sedimentary burial; Triassic surface temperatures have been set to 25 °C [96].
(3)   late Paleozoic peneplanation with subsequent late Paleozoic–early Mesozoic burial beneath sediments, followed by rapid cooling in the Late Triassic–Early Jurassic and renewed burial in the Jurassic (as suggested by studies from adjacent regions by e.g., Krohne [13] and Sirevaag et al. [14]). This has been implemented by forcing the samples to the surface in the Early Jurassic, assuming a surface temperature of 25 °C, corrected for each sample's depth below the extrapolated peneplain, followed by a second constraint box to allow for re-burial.

5. Results

The fission track and (U-Th)/He analyses are summarized in Appendices A and B, as well as Figures 4 and 5. Apatite fission track single-grain ages are reported in Supplementary Material Table S1, while track length data are reported in Supplementary Material Table S2 and Figure S1.

5.1. Apatite Fission Track Results

Thirty-one samples were selected for apatite fission track analyses. The uranium concentrations range from c. 5 to 98 ppm, with most apatites showing relatively homogeneous uranium distribution. The average measured Dpars, which are used as a proxy for apatite annealing kinetics, range from

c. 1.2 to 1.8 μm. Most of the Dpars are lower than 1.6 μm, representing fast-annealing near-end member fluorapatites [97]. There are no observed correlations of age to either Dpar or to uranium concentration within the dataset.

The AFT ages range from c. 280 to 85 Ma, although the majority of the ages are either Cretaceous (n = 14) or Jurassic (n = 10). Measured confined track lengths (MTL) span from c. 10.3 to 13.4 μm, with all but six samples recording MTLs longer than 11.3 μm.

The AFT ages younger than c. 165 Ma are mainly derived from elevations below c. 1500 m a.s.l., whereas ages older than c. 165 Ma are mostly found at higher elevations (Figure 4A). This results in a moderate correlation (R^2 = 0.5) between age and elevation for all samples excluding the samples from Schirmacheroasen. Additionally, a regional trend is observed when plotting AFT data against latitude (Figure 4B), with younger ages close to the coast and older ages towards the great escarpment. Since elevations also increase towards the inland, it is difficult to determine whether elevation or distance from the coast, or both, control the distribution of fission track ages.

The age–MTL plot (Figure 4C) shows mainly two groups of samples. The majority of samples have mean track lengths above 11.3 μm and cover the entire range of ages, whereas six samples with mean track lengths below 11.3 μm mostly cluster around 150 Ma. The samples from this latter group were all collected below c. 1800 m a.s.l. and south of c. 71° S (Figure 4D).
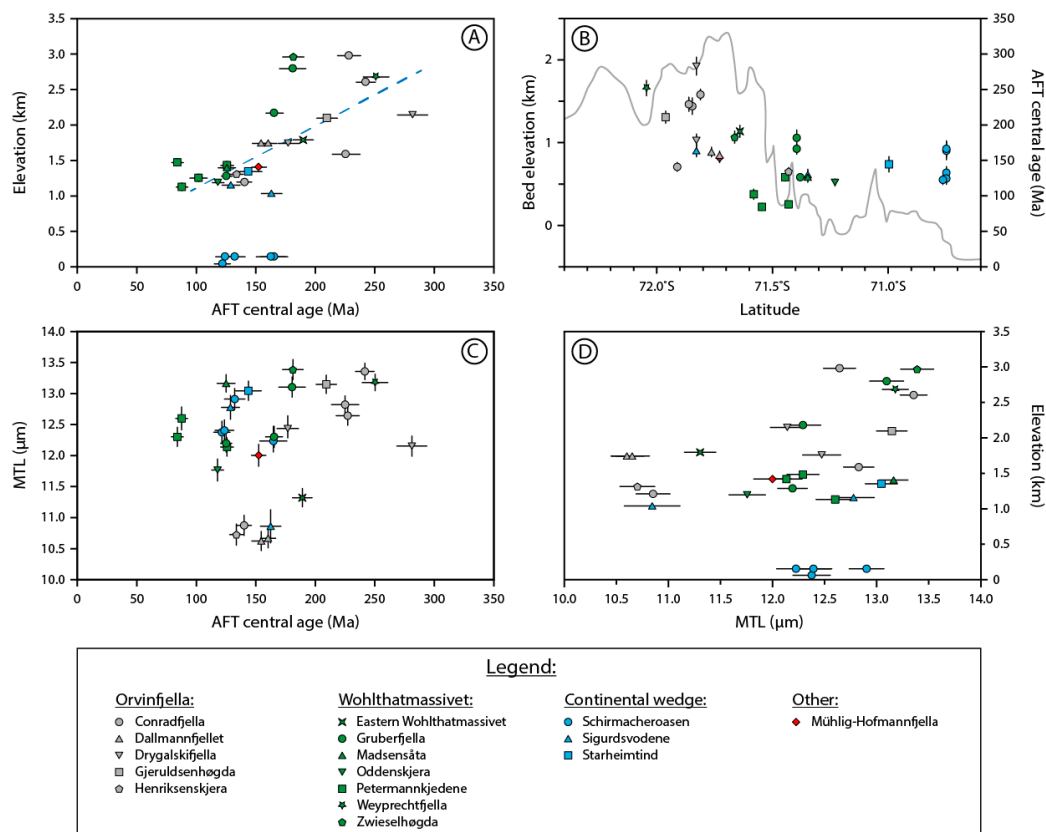

Figure 4. Apatite fission track ages from 31 samples. Reported errors for AFT ages are 1σ, whereas the track length errors are given as 1SE. (**A**) AFT ages up to c. 165 Ma are generally found below c. 1500 m a.s.l., while AFT ages above c. 165 Ma are found above. All samples, except samples from Schirmacheroasen, produce a moderate age–elevation relationship. (**B**) AFT ages correlate with latitude, showing generally younger ages towards the coast. A cross section of the topography from the hinterland to the coastline at c. 11 °E is shown in gray. (**C**) A small group of samples with mean confined track lengths below 11.3 μm are clustered between c. 135 and 190 Ma, while samples with longer track lengths cover the entire age range. (**D**) Track lengths longer than 11.3 μm are obtained from elevations up to c. 3000 m a.s.l., whereas shorter track lengths are limited to elevations below c. 1800 m a.s.l.

5.2. (U-Th)/He Results

(U-Th)/He analyses were conducted on 132 apatite crystals from 33 samples. The selected crystals were mostly euhedral and of good quality. Some of the selected crystals contained small inclusions and fractures even though considerable effort was put into selecting the best possible grains for analyses. The calculated sphere radii are between 31 and 122 μm, although most grains are smaller than c. 100 μm. Most of the samples have effective uranium (eU) concentrations up to c. 240 ppm. However, extremely high eU concentrations are recorded in all five grains from sample JJ1875 (Madsensåta), with eU concentrations ranging from 780 to 1812 ppm.

Fourteen of the 132 single-grain analyses were excluded according to the filtering criteria described in Section 4.2. Eleven single-grain ages were statistical outliers compared to the rest of the single-grain analyses of the specific sample, and were thus excluded. Two analyses were excluded due to large error, and one analysis was excluded because the age was significantly older than all AFT and ZHe ages of the study area.

The remaining apatite (U-Th)/He analyses gave single-grain ages between c. 305 and 15 Ma. Similar to the AFT data, the AHe ages correlate moderately well ($R^2 = 0.5$) with elevation (Figure 5A) and are generally younger towards the coast to the north (Figure 5B).
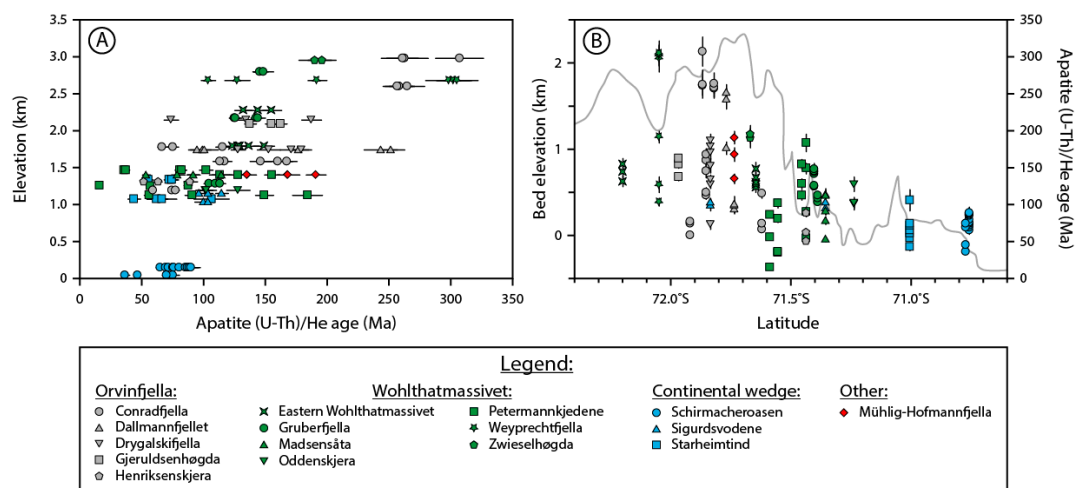

Figure 5. Apatite (U-Th)/He data from 33 samples. Reported errors are 1σ. (**A**) Single-grain apatite (U-Th)/He ages correlate moderately well with elevation. (**B**) The apatite (U-Th)/He analyses yield progressively older ages towards the inland, similar to the apatite fission track analyses. A topographic cross section as in Figure 4 is included in gray.

The (U-Th)/He data have been evaluated based on the scatter of single-grain ages within a sample. The standard deviation of the single-grain ages is below 10% for 15 of our samples and between 10 and 20% for eight samples; ten samples have standard deviations exceeding 20%. Some scatter in single-grain ages can be expected, even though the individual grains in a sample have experienced similar *t–T* histories. To some extent, this can be explained by grain characteristics, such as grain size, radiation damage, eU zonation, U–Th-rich micro-inclusions and He-implantation from neighboring grains [98–101]. Large apatites are expected to yield older ages than smaller apatites since the larger apatites have greater effective diffusion dimensions, and thus higher He retentivities [100]. Also, as the accumulation of radiation damage reduces the diffusivity of He in apatites, it is expected that high-eU apatites will yield older ages than low-eU apatites [77]. Thus, a positive relationship for both age–eU and age–grain size can explain the scatter of single-grain ages within a sample. For samples where a 1σ standard deviation above 20% cannot be explained by either age–eU or age–grain size relationships, Flowers and Kelley [101] suggest to exclude the apatite (U-Th)/He data from the thermal modelling. From the ten samples with a standard deviation above 20%, six samples show a moderate to very good correlation ($R^2 > 0.6$) between either age–eU, age–grain size or both, and are therefore included in the

models. In the remaining four samples (JJ1677, JJ1875, JJ1924 and JJ1974) ages do not correlate with eU or grain size ($R^2 < 0.2$), and the samples are thus excluded from modelling.

Zircons from two samples, both from Schirmacheroasen, were analyzed by the (U-Th)/He method. This resulted in six single-grain ages ranging from c. 420 to 340 Ma. The calculated sphere radii range from 47 to 55 μm, while measured eU concentrations are between 130 and 339 ppm. None of the zircon (U-Th)/He analyses were rejected. The single-grain zircon (U-Th)/He ages show a standard deviation of 2 and 7% for the two different samples.

By combining apatite fission track with apatite and zircon (U-Th)/He data, the thermal evolution of a sample can be traced through a wide temperature range (c. 230–35 °C). The obtained thermochronological age corresponds to the cooling through the partial annealing/retention zones of the different thermochronometers. Based on the partial annealing/retention zones of the different systems, we would expect the ZHe age to be oldest (PRZ: c. 230–150 °C; [76]), followed by the AFT age (PAZ: c. 120–60 °C; [74]) and the AHe age (PRZ: c. 70–35 °C; [75]). For the 31 multidated samples in this study, the ZHe age is the oldest in both cases. While the AHe ages of most samples are younger than the corresponding AFT ages, five samples yielded similar unweighted mean apatite (U-Th)/He ages and apatite fission track ages, meaning that the ages either overlap within their uncertainties or the fission track age overlaps with the range of single-grain (U-Th)/He ages. In three other samples, all apatite (U-Th)/He single-grain ages are older than the fission track age. These samples are all older than 160 Ma (AFT age) and have U concentrations above 30 ppm (Appendix A). Samples with similarly high (or higher) U but younger AFT ages do not show a crossover in age, thus we consider this to be an effect of radiation damage accumulation over time.

6. Tectono-Thermal Evolution

During the Pan-African orogeny, various parts of East- and West Gondwana collided to form the Himalaya-scale East African-Antarctic Orogen and the supercontinent Gondwana, e.g., [31]. The collapse of this orogen and eventual breakup of Gondwana in Jurassic-Cretaceous times, gave birth to our modern oceans. Central Dronning Maud Land was in the thick of these momentous events and preserves excellent evidence of the collisional history and early orogenic collapse, e.g., [29]. The geological record of rifting, continental breakup and the transformation into a passive continental margin, on the other hand, has been lost to subsequent erosion, and the only post-Pan-African rocks exposed in central Dronning Maud Land are a few mafic dykes associated with the Jurassic Karoo flood basalt province [60,61]. In the absence of geological evidence to the contrary, previous authors have interpreted thermochronological data from central Dronning Maud Land in the context of a relatively simple history of protracted cooling from Late Cambrian times until today, e.g., [8–10]. Significantly more complex thermal histories have since been proposed for areas east and west of central Dronning Maud Land and cast doubt on this simple model [12–14]. Testing such a simple cooling model against our data has failed to produce any acceptable cooling paths in about half the samples (Appendix C). Samples that are incompatible with protracted cooling can be found all over the study area, confirming that this scenario is likely too simple and more complex thermal histories should be investigated (Figures 6–8). Considering the scarcity of a post-Pan-African geological record in central Dronning Maud Land, we will have to look towards adjacent regions in western and eastern Dronning Maud Land and towards South Africa-Mozambique, the conjugate margin to central Dronning Maud Land, to develop reasonable geological scenarios that can be tested against our data.

6.1. Post-Pan-African Evolution

6.1.1. Late Paleozoic–Early Mesozoic Peneplanation and Sedimentary Basins

The oldest post-Pan-African geological feature preserved in Dronning Maud Land is a distinct erosional unconformity separating Mesoproterozoic basement rocks from the overlying upper Carboniferous–Middle Permian Beacon sediments. This erosional surface, interpreted as an ancient

peneplain, can be observed in Heimefrontfjella, Kirwanveggen and Fossilryggen in western Dronning Maud Land [42]. Additionally, remnants of a similar paleosurface have been reported from Gjelsvikfjella (western Dronning Maud Land; [47]) and Sør-Rondane (eastern Dronning Maud Land; [13,48,49]). Though lacking the overlying sediments, these paleosurfaces have been correlated with the peneplain exposed in western Dronning Maud Land. In the Transantarctic Mountains, c. 800 km west of Dronning Maud Land, the Beacon sediments (Devonian–Triassic) also cover an erosional unconformity, the Kukri erosional surface [45]. This distinct Devonian–Carboniferous paleosurface or peneplain below the Beacon sediments can therefore be traced over hundreds of kilometers, from the Transantarctic Mountains far to the west of our study area to Sør-Rondane to the east of our study area. While this paleosurface is less well preserved in central Dronning Maud Land, peneplains are large-scale features [102] and we consider it likely that the same erosional surface was once present in our study area as well; it must today mostly lie above the present-day erosional level. Mountain tops from the crest of the escarpment to the hinterland can be linked by an enveloping surface with a gentle southward dip of c. 1°, and we speculate that this enveloping surface represents the last remnant of the once continuous Devonian–Carboniferous peneplain that truncated all of Dronning Maud Land.

Peneplanation was followed by subsidence and sedimentation. Only erosional remnants of the Beacon sediments are preserved in western Dronning Maud Land, but a more complete succession of 2.5–3 km thick Devonian-Triassic Beacon sediments can be found in the Transantarctic Mountains [43–45]. In Mozambique and South Africa, the upper Carboniferous–Lower Jurassic Karoo sediments are considered to be equivalent to the Beacon Sediments and are still preserved in thicknesses of 4–4.5 km and 12 km, respectively [46,103–105]. Western Dronning Maud Land was thus surrounded by upper Paleozoic–lower Mesozoic sedimentary basins, suggesting that equivalent sediments might have been deposited in our study area as well. Indeed, all apatite (U-Th)/He and fission track ages are Permian or Mesozoic, thus a late Paleozoic peneplanation, bringing the samples close to the surface, must have been followed by reburial to account for the younger ages.

Most of our samples are Jurassic and younger and do not record the late Paleozoic–early Mesozoic history. Thus, we have selected three of the oldest samples, yielding Triassic ages (JJ1720, JJ1736 and JJ1746), and two samples from Schirmacheroasen, for which ZHe ages are also available (J03.02./1 and S30.1), to investigate potential peneplanation and subsequent re-burial. All five samples allow late Paleozoic cooling to (near) surface temperatures, followed by re-heating due to sedimentary burial. Temperatures during burial must have reached at least 80 °C during Permo-Triassic times (Figures 6 and 8). The maximum temperatures are not well constrained; most good-fit paths suggest temperatures between c. 80–140 °C, corresponding to at least c. 3 km, but possibly up to c. 6 km of sediments (assuming a geothermal gradient of c. 25 °C). These estimates, though vague, agree with recorded Beacon and Karoo sediment thicknesses in the Transantarctic Mountains, Mozambique and South Africa. The depth of the samples from Schirmacheroasen below the late Paleozoic peneplain is uncertain. These samples come from coastal outcrops far north of the escarpment and the peneplain might have been kilometers above the present-day erosional level or might have been downfaulted or downwarped during rifting [106]. The two models from Schirmacheroasen indicate similar temperatures during peneplanation and burial than samples from the main mountain range and thus might have been at a similar crustal depth in the late Paleozoic–early Mesozoic. With thousands of meters difference in elevation today, down-to-the-north faulting along margin parallel normal faults during rifting seems the most likely possibility.

The samples with Jurassic and younger AFT and AHe ages have lost all information about the late Paleozoic–early Mesozoic thermal history. We assume, however, that they have experienced peneplanation and subsequent sedimentation as well, as these are not local, but usually rather widespread phenomena that should affect the entire study area. Thus, we have applied the information on peneplanation and sedimentary burial that we have gained from the five samples discussed above as external constraints to all the models for younger samples. We would like to point out that all samples are compatible with late Paleozoic–early Mesozoic peneplanation and burial (Appendix C),

thus we prefer this scenario over a simple cooling history as discussed above, which failed to produce even acceptable-fit cooling paths in half the samples.
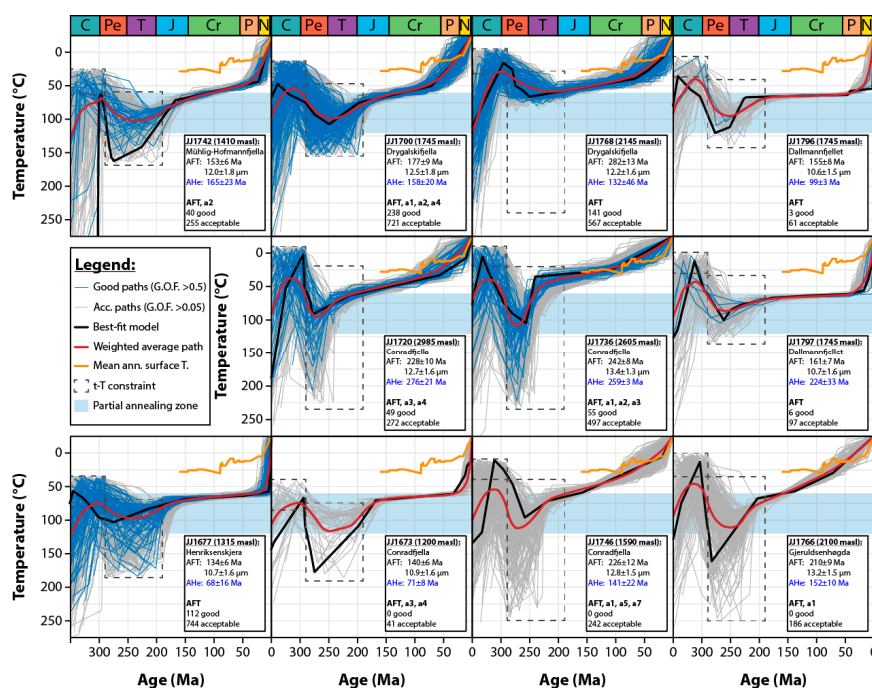

Figure 6. Time–temperature paths generated by the HeFTy software [89] for Orvinfjella and Mühlig-Hofmannfjella. 100,000 random paths were tested for each sample. For each sample, AFT central age and mean track length (black) are reported with 1σ error. AHe age (blue) is given as unweighted mean age with 1σ error. Below that: (1) In bold, the thermochronometers included in the specific thermal model; the "a" numbers indicate the considered AHe single-grain analyses. (2) The number of good and acceptable paths found for each model. Good fits represent goodness-of-fit ≥0.5, while acceptable fits correspond to goodness-of-fit ≥0.05. Mean annual surface temperatures after Barrett [107], Poole et al. [108], Thorn and DeConto [109] and Jenkyns et al. [110].
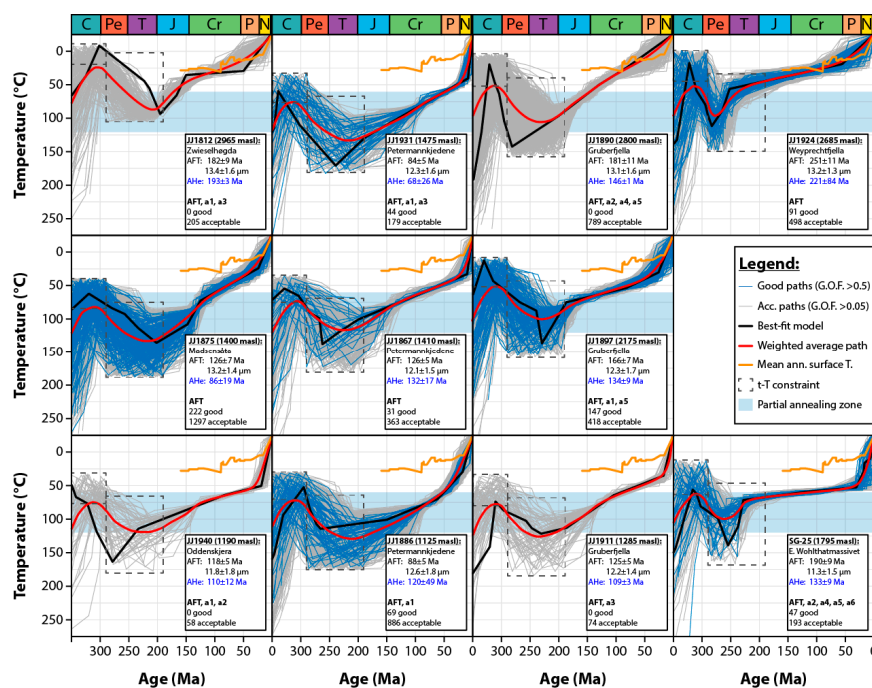

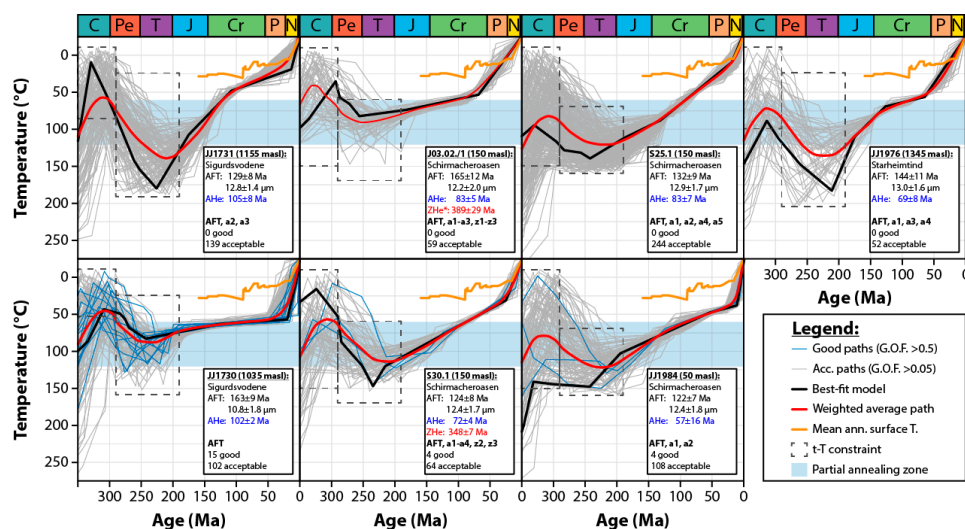**Figure 7.** Modelled thermal histories of samples from Wohlthatmassivet. For explanations, see Figure 6.

Figure 8. Modelled thermal histories from the continental wedge samples. ZHe age (red) is given as unweighted mean age and 1σ error. * ZHe data included for modelling of sample J03.02./1 are from sample J02.02./2 at the same locality. For further explanations, see Figure 6.

6.1.2. Jurassic Reburial?

In Heimefrontfjella (western Dronning Maud Land), the Beacon sediments have been eroded down to a few meters, before being covered by up to 1.5–2 km of Jurassic continental flood basalts, indicating that the basement rocks exposed today were already close to the surface twice before, first during the Carboniferous–Permian deposition of the Beacon sediments and then again during the Early Jurassic emplacement of the continental flood basalts [14,42]. These flood basalts were associated with early Gondwana rifting and extended at least as far east as Hochlinfjellet in western Dronning Maud Land. Apatite fission track data from that region indicate diminishing basaltic thicknesses away from the emplacement zone in Jutulstraumen [14]. Today, the only evidence for the Karoo magmatism in central Dronning Maud Land are Jurassic mafic dykes in Petermannkjedene [60] and Schirmacheroasen [61]. In order to further pinpoint the extent of the continental flood basalts, we tested the westernmost of our samples from the main mountain range (JJ1700, JJ1742 and JJ1768) for Early Jurassic surface exposure and rapid reheating due to burial beneath flood basalts. While all three samples might have cooled to (near) surface temperatures already in Early Jurassic times, none of the models showed signs of Jurassic reheating (Appendix C). The models were not forced to higher temperatures in the Jurassic, but a relatively large constraint box was used, allowing samples to either stay at (near) surface temperatures or be reheated due to burial. The absence of Jurassic reheating in these samples leads us to suggest that the eastern margin of the Jurassic continental flood basalts was located somewhere between Hochlinfjellet (4° E) and Mühlig-Hofmannfjella (7° E).

Other areas in East Antarctica have been buried beneath Jurassic sedimentary basins (Sør-Rondane: [13]; Victoria Basin: [111]; Shackleton Range: [112]). We have thus tested a similar scenario (late Paleozoic peneplanation, burial beneath the Beacon sediments, erosion of Beacon sediments, burial beneath Jurassic basin) against our data. However, the majority of our samples either do not favor Jurassic reheating (significantly fewer good- or acceptable-fit paths are found than for models without Jurassic reheating, e.g., samples JJ1796, JJ1812, SG-25; Appendix C)) or do not show any significant increase in temperature during the Jurassic (e.g., samples JJ1700, JJ1736, JJ1730; Appendix C). Several models allow for Jurassic reheating, simply because the thermochronological ages are Cretaceous and the samples essentially preserve little to no information on the Jurassic thermal history (e.g., samples JJ1886, JJ1931, JJ1875, JJ1731). None of these models actually requires Jurassic–Cretaceous reheating and they all work equally well without it. Our modelling results might therefore allow for a few relatively local, shallow sedimentary basins, but we do not believe that entire central Dronning Maud Land was covered by a thick section of Jurassic or younger sediments.

6.1.3. Mesozoic–Cenozoic Cooling

The Mesozoic-Cenozoic thermal evolution of central Dronning Maud Land is generally characterized by relatively slow cooling until the onset of glaciation (Figures 6–8). During Jurassic to early Paleogene times, average cooling rates were well below 1.0 °C/Myr for most samples. A significant change in cooling rates can be observed at the Eocene–Oligocene boundary, with average cooling rates of c. 0.7–2.6 °C/Myr being recorded during the last 34 Ma. Temporarily, cooling rates reached up to c. 7.5 °C/Myr, e.g., in Orvinfjella. The cooling rates since Oligocene times are similar to the cooling rates recorded in western Dronning Maud Land during the glaciation [14].

Throughout the Paleogene, the southward drift of Antarctica resulted in a progressively more isolated position of the continent. This led to the transition from a temperate–cool subtropical climate during the Early Eocene, to cooling and eventually glaciation around the Eocene–Oligocene boundary [70,113–115]. The dramatic decrease in temperature due to the changing climate (from 25 °C surface temperatures in the Late Cretaceous to −25 °C surface temperature today) is large enough to be recorded in low-temperature thermochronological data. At the same time, the deteriorating climate and eventual onset of glaciation marked a significant change in weathering and erosion conditions, enhancing denudation and cooling. To differentiate between the two, we compare the modelled temperatures of our samples with the surface temperature curve since Late Jurassic times. Interestingly, several samples from Orvinfjella, Wohlthatmassivet and Weyprechtfjella reached surface temperatures already in the Late Jurassic (JJ1736 and JJ1924) or during the Cretaceous (JJ1700, JJ1720, JJ1746, JJ1766, JJ1768 and JJ1812). The cooling histories of these particular samples more or less follow the surface temperature curve throughout the Cenozoic, indicating that the samples were sitting close to the surface and apparently experienced no significant Cenozoic erosion; the Cenozoic cooling in these models is entirely attributed to climate cooling. All other samples, on the other hand, show greater Cenozoic cooling than can be explained by the changing climate and we attribute this cooling to erosion of the overlying rock column. Freeze-thaw processes, especially during the early stages of glaciation, are a highly effective mechanism for physical weathering [116] and the offshore sedimentary record, which is dominated by Cenozoic sediments, also supports this interpretation. Additionally, Cenozoic faulting might have contributed to Cenozoic cooling by tectonic denudation. However, the continental margin has been a passive-margin since Cretaceous rifting and we expect fault activity to have played a minor role at most. Comparing the modelled temperatures of samples at the onset of glaciation to the surface temperatures and applying a geothermal gradient of 25 °C/km, we can estimate the paleodepth of the samples and hence the eroded rock column since the onset of glaciation. Many samples from the continental wedge and Orvinfjella were located at relatively shallow crustal depths at the onset of the glaciation (< 500 m), indicating that most of the erosion must have taken place prior to 34 Ma. Several samples from the main mountain range (e.g., JJ1673, JJ1796, JJ1931), on the other hand, experienced up to 2 km of erosion in the last 34 Ma. Erosion was thus strongly focused, which is to be expected from glacial erosion processes.

6.2. Regional Thermochronological Age Distribution and Tectonic Implications

A comparison of the published apatite fission track ages from Dronning Maud Land reveals important differences between western, central and eastern Dronning Maud Land (Figure 9). While peaks in the age distribution should be regarded with caution, since fission track ages in slowly cooled samples do not necessarily correspond to any particular geological event, the differences are also evident in age-elevation plots and modelled cooling histories. As a first observation, the proportion of ages pre-dating the Jurassic onset of rifting seems to increase from west to east. Jurassic rifting was associated with the eruption of voluminous continental flood basalts in western Dronning Maud Land and burial beneath these basalts reset most of the low-temperature thermochronometers. Older ages only survived in areas where the basaltic cover was relatively thin, e.g., in easternmost western Dronning Maud Land [14]. Central and eastern Dronning Maud Land were most likely never covered by basalts and thus preserve better evidence of the pre-rift history.

In eastern Dronning Maud Land, the Late Triassic–Early Jurassic and Late Jurassic–Early Cretaceous age peaks generally correspond to periods of cooling recorded in the thermal history models from that area, and have been linked to early rift processes in Gondwana and rifting in the Riiser-Larsen Sea, respectively [13]. In central Dronning Maud Land, the Jurassic and Cretaceous age peaks do not correlate with any significant cooling episodes in the thermal models, suggesting that these ages might not record any particular geological event but rather reflect relatively slow cooling through the partial annealing zone. This is also indicated by the age-elevation distribution in central Dronning Maud Land, where Permian to Cretaceous fission track ages are clearly correlated with elevation, with a gentle slope indicative of slow Mesozoic cooling (excepting samples from Schirmacheroasen, which was most likely downfaulted with respect to the main mountain range). This is a marked contrast to western Dronning Maud Land, where mid-Cretaceous ages clearly dominate the age spectrum and occur over a wide range of elevations (c. 900–2400 m a.s.l.), suggesting rapid cooling at this time. The latter is reflected in increased Cretaceous cooling rates recorded in many of the thermal history models from western Dronning Maud Land.
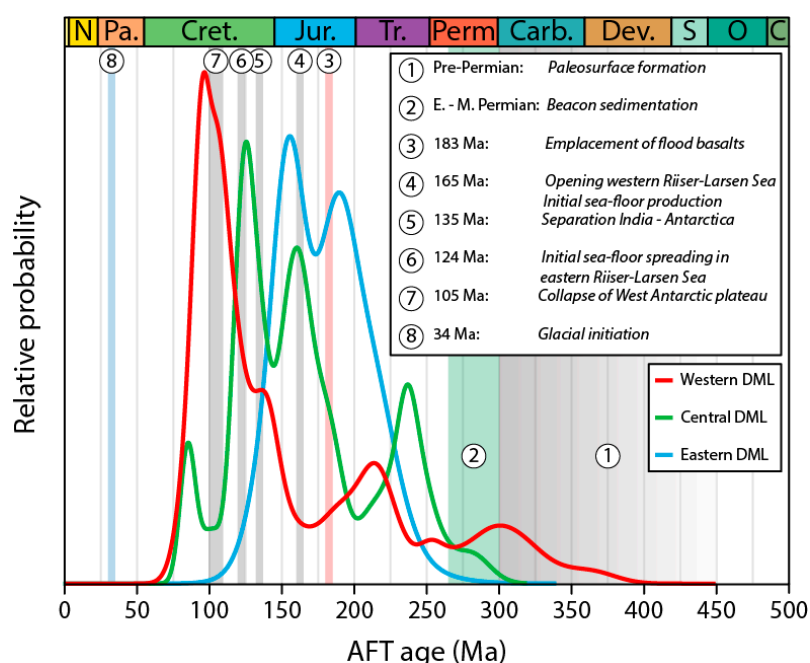

Figure 9. Probability density plot generated from available apatite fission track central ages from Dronning Maud Land. The time range of the main events that potentially affected the region are indicated in the background. The AFT ages from western Dronning Maud Land (DML) include data from Jacobs and Lisker [11], Emmel et al. [12] and Sirevaag et al. [14]. AFT ages from central Dronning Maud Land include the data from the present study together with the data from Emmel et al. [10]. The AFT ages from eastern Dronning Maud Land are solely based on data from Krohne [13]. Timing of the different events are from Plumstead [38], Lindström [40,41], Isbell [45], Duncan et al. [50], Roeser et al. [62], Bialas et al. [67] and Ingólfsson [114].

Comparing the thermal history models from western and central Dronning Maud Land, we suggest that samples from both areas were most likely close to the surface during the late Paleozoic peneplanation and were subsequently buried beneath upper Paleozoic–lower Mesozoic sedimentary basins. Inversion of these basins and erosion of the sediments occurred relatively quickly during Early Jurassic times in western Dronning Maud Land and much slower during Jurassic–Cretaceous times in central Dronning Maud Land. This difference might be explained by dynamic uplift above the Karoo mantle plume starting at ca. 200 Ma, which affected western Dronning Maud Land, but did not extend as far east as central Dronning Maud Land. The eruption of a thick layer of Jurassic flood basalts associated with this plume then preserved the remnants of Carboniferous–Permian Beacon sediments

that can still be found in western Dronning Maud Land today, while the unshielded sediments in central Dronning Maud Land have since been completely stripped by erosion.

The pronounced Cretaceous cooling in western Dronning Maud Land has been linked to rift processes in the South Atlantic and Riiser-Larsen Sea, passive continental margin development and climate change [14]. Its absence in central Dronning Maud Land, however, suggests that it might have more local sources. To the west, in the area of the West Antarctic Rift System, an orogenic plateau with strongly thickened crust had developed during long-lasting subduction along the Panthalassic margin of Gondwana [67,117,118]. This plateau existed until mid-Cretaceous times, when the subduction on the Pacific margin ceased ([119]; and references therein), leading to plateau collapse at c. 105 Ma and the development of the West Antarctic Rift System and the present-day Transantarctic Mountains [67]. The age of plateau collapse coincides well with the main age peak recorded in western Dronning Maud Land and the relative proximity of western Dronning Maud Land to the West Antarctic Rift System might explain the pronounced mid-Cretaceous cooling recorded here and lack thereof in areas further east.

7. Summary and Conclusions

We have applied a combination of low-temperature thermochronological methods (i.e., apatite fission track, apatite and zircon (U-Th)/He) to gain insights into the post-Pan-African evolution of central Dronning Maud Land. While previous studies from central Dronning Maud Land have interpreted thermochronological data in terms of simple, monotonic post-Pan-African cooling, our thermochronological data suggest a more complex tectono-thermal history. We have tested models including late Paleozoic peneplanation and subsequent re-burial beneath the Beacon sediments, as well as models that additionally include Early Jurassic erosion followed by a second period of Mesozoic re-burial. Whereas a second period of surface exposure and subsequent burial is favored in western and eastern Dronning Maud Land, the new data are most consistent with a scenario that only includes late Paleozoic (near) surface exposure and late Paleozoic–early Mesozoic re-burial by c. 3–6 km of Beacon sediments. Also, as the westernmost samples do not show signs of Jurassic re-burial beneath continental flood basalts, the eastern boundary of the Jurassic continental flood basalts can be pinpointed to the area between Hochlinfjellet (4° E) and Mühlig-Hofmannfjella (7° E).

Contrary to eastern and western Dronning Maud Land, the AFT age peaks in central Dronning Maud Land do not correlate to any particular cooling phases in the thermal models. Combined with a gently sloping AFT age–elevation correlation for all central Dronning Maud Land samples, except for Schirmacheroasen (which was probably downfaulted), this indicates slow cooling throughout the Mesozoic ($\leq$1 °C/Myr). The lack of a pronounced Cretaceous cooling phase as observed in western Dronning Maud Land, suggests that the mid-Cretaceous cooling of western Dronning Maud Land [14] could be attributed to the proximity to the collapse of the orogenic plateau at the Panthalassic Gondwana margin at c. 105 Ma, and the following formation of the West Antarctic Rift System, rather than to rift processes in the South Atlantic and the Riiser-Larsen Sea. Since the Paleogene, increased cooling rates are attributed to climate deterioration and glacial denudation of up to 2 km.

Appendix A

Table A1. Apatite fission track data from central Dronning Maud Land.

Sample	Region	Elev. [m]	Sample Quality	n (G)	Spontaneous ρs	Ns	Induced ρi	Ni	ρd	Nd	P(χ²) [%]	Disp.	U [ppm]	Dpar [μm]	±1σ [μm]	Central Age [Ma]	±1σ [Ma]	Measured MTL [μm]	±1σ [μm]	C-Axis Proj. MTL [μm]	±1σ [μm]	n (G)
	Mühlig-Hofmannfjella																					
JJ1742	Mühlig-Hofmannfj.	1410	G, f	20	41.51	1689	57.19	2327	19.872	35707	49	0.02	45	1.30	0.11	153	6	12.0	1.8	13.3	1.3	100
	Orvinfjella																					
JJ1700	Drygalskifjella	1745	G	20	19.85	960	23.60	1141	19.984	35707	55	0.01	18	1.49	0.12	177	9	12.5	1.8	13.2	1.3	100
JJ1768	Drygalskifjella	2145	F, f, wz/z	20	39.91	1720	29.38	1266	19.817	35707	65	0.01	22	1.28	0.08	282	13	12.2	1.6	13.4	1.2	100
JJ1673	Conradfjella	1200	F, z	20	30.60	2522	46.98	3872	20.208	35707	0	0.12	40	1.48	0.12	140	6	10.9	1.6	12.5	1.2	100
JJ1720	Conradfjella	2985	G	20	82.07	3856	68.92	3238	18.199	41977	0	0.11	53	1.41	0.11	228	10	12.7	1.6	13.8	1.1	100
JJ1736	Conradfjella	2605	VG, (f), (i)	20	57.31	4447	45.35	3519	18.262	41977	83	0.00	35	1.40	0.09	242	8	13.4	1.3	14.3	1.0	100
JJ1746	Conradfjella	1590	G	20	20.04	1606	18.91	1378	18.325	41977	4	0.11	15	1.33	0.07	226	12	12.8	1.5	13.9	1.1	100
JJ1766	Gjeruldsenhøgda	2100	G, f, (z)	20	24.72	1883	22.79	1736	18.388	41977	91	0.00	19	1.35	0.09	210	9	13.2	1.5	14.2	1.1	100
JJ1796	Dallmannfjellet	1745	G, f, wz/z	20	24.29	1188	22.54	1591	19.761	35707	19	0.09	26	1.31	0.07	155	8	10.6	1.5	12.6	1.1	100
JJ1797	Dallmannfjellet	1745	F, z	20	32.07	1691	31.47	2187	19.649	35707	18	0.09	34	1.37	0.09	161	7	10.7	1.6	12.3	1.2	86
JJ1677	Henriksenskjera	1315	G, z	20	39.09	1903	62.12	3024	20.152	35707	16	0.07	52	1.41	0.06	134	6	10.7	1.6	12.4	1.1	89
	Wohlthatmassivet																					
JJ1812	Zwieselhøgda	2965	F, z	20	25.82	1049	29.39	1194	19.593	35707	77	0.01	25	1.37	0.15	182	9	13.4	1.60	14.3	1.2	100
JJ1838	Petermannkjedene	1260	F, i	20	4.62	388	9.94	835	20.432	35707	59	0.09	8	1.24	0.07	102	7	-	-	-	-	-
JJ1867	Petermannkjedene	1410	F, i	20	32.85	1351	54.03	2222	19.537	35707	66	0.00	41	1.35	0.08	126	5	12.1	1.5	13.4	1.1	100
JJ1886	Petermannkjedene	1125	F, f	20	15.58	744	34.83	1663	18.514	41977	24	0.11	28	1.27	0.09	88	5	12.6	1.8	13.7	1.5	100
JJ1931	Petermannkjedene	1475	G	20	11.69	518	27.47	1217	18.577	41977	48	0.02	22	1.30	0.09	84	5	12.3	1.6	13.5	1.3	100
JJ1875	Madsensåta	1400	F, f, (wz)	20	74.86	2271	118.93	3608	18.640	41977	0	0.20	98	1.63	0.12	126	7	13.2	1.4	14.1	1.1	100
JJ1890	Gruberfjella	2800	F, f	20	25.45	1073	30.36	1280	20.300	36879	1	0.16	22	1.42	0.12	181	11	13.1	1.6	14.1	1.2	100
JJ1897	Gruberfjella	2175	F, (f), (i)	20	22.64	1739	29.36	2256	20.249	36879	10	0.07	21	1.35	0.08	166	7	12.3	1.7	13.6	1.2	100
JJ1911	Gruberfjella	1285	F	20	61.79	3150	105.51	5379	20.197	36879	5	0.07	81	1.50	0.12	125	5	12.2	1.4	13.4	1.1	100
JJ1924	Weyprechtfjella	2685	G, (f)	20	44.55	1854	33.76	1405	18.136	41977	77	0.00	27	1.39	0.09	251	11	13.2	1.3	14.2	1.0	100
JJ1940	Oddenskjera	1190	F, f, z, i	20	31.41	1868	55.17	3281	19.481	35707	22	0.07	45	1.40	0.11	118	5	11.8	1.8	13.2	1.3	100
SG-25	E. Wohlthatmassiv.	1795	F, f, d	23	35.38	1726	37.81	1845	19.201	35707	15	0.08	30	1.46	0.08	190	9	11.3	1.5	12.8	1.2	100
	Continental wedge																					
JJ1730	Sigurdsvodene	1035	G	20	11.40	886	14.72	1144	19.928	35707	43	0.06	11	1.41	0.08	163	9	10.9	1.8	12.4	1.2	47
JJ1731	Sigurdsvodene	1155	G, (f)	20	8.69	575	13.17	871	18.451	35707	65	0.00	10	1.26	0.05	129	8	12.8	1.4	13.9	1.0	47
JJ1976	Starheimtind	1345	F, f	20	8.39	463	11.76	649	18.703	41977	16	0.15	9	1.48	0.10	144	11	13.1	1.6	14.0	1.3	100
JJ1984	Schirmacheroasen	50	F, (i)	20	13.22	802	22.42	1360	19.425	35707	17	0.10	17	1.58	0.11	122	7	12.4	1.8	13.6	1.3	100
S25.1	Schirmacheroasen	150	G, (d)	20	9.61	474	14.84	732	19.313	35707	63	0.01	11	1.77	0.09	132	9	12.9	1.7	14.0	1.3	100
S30.1	Schirmacheroasen	150	G	21	14.17	734	23.40	1212	19.257	35707	6	0.15	18	1.53	0.12	124	8	12.4	1.7	13.6	1.2	100
J02.02/2	Schirmacheroasen	150	G	20	10.00	477	13.54	646	20.655	35707	9	0.15	9	1.39	0.15	163	13	-	-	-	-	-
J03.02/1	Schirmacheroasen	150	G	20	5.89	500	7.79	661	20.599	35707	29	0.12	5	1.50	0.07	165	12	12.2	2.0	13.4	1.5	100

Table footnote: n(G): number of dated grains; n(TL): number of measured track lengths; $N_{s,i,d}$: number of spontaneous (N_s) and induced (N_i) tracks and number of tracks counted on dosimeter glass IRMM-540R (N_d); $\rho_{s,i,d}$: track densities (1×10^5 tracks cm^{-2}) of spontaneous (ρ_s) and induced (ρ_i) tracks and on dosimeter glass IRMM-540R (ρ_d); P(χ^2): p-value of the chi-square homogeneity test [98]; Disp.: dispersion; U: uranium concentration; Dpar: etch pit diameter; MTL: mean track length. Sample quality: VG: very good; G: good; F: fair; d: dislocations; f: fractures; i: inclusions; z/ wz: zoned/ weakly zoned. Letters in brackets correspond to grain features that only affect few grains in the sample. Fission track analyses are conducted by H. Sirevaag ($\zeta_{\text{IRMM-540R}}$ = 214 ± 5).

Appendix B

Table A2. Apatite and zircon (U-Th)/He analyses.; Excluded analyses are marked in italic. The reason for exclusion is given in the last column of the table.

Sample	Term	SR [µm]	He Vol. [ncc]	He 1σ [%]	He Mass [ng]	He 1σ [%]	238U Conc. [ppm]	238U 1σ [%]	238U Mass [ng]	232Th 1σ [%]	232Th Conc. [ppm]	Th/U ratio	Sm Mass [ng]	Sm 1σ [%]	Sm Conc. [ppm]	eU [ppm]	Ejec. Corr. (fT)	Uncorr. He-Age [Ma]	FT Corr. He-Age [Ma]	1σ [Ma]	Unweighted Sample Average Age [Ma]	1σ [Ma]	Reason for Exclusion
JJ1742 a1	2	49	2.847	1.1	0.132	1.9	31.1	2.5	0.153	2.4	35.8	1.15	4.62	6.8	1084	39	0.67	113	168	9			
JJ1742 a2	2	54	3.603	1.0	0.195	1.9	39.4	2.4	0.284	2.4	57.4	1.46	6.33	6.8	1279	53	0.70	94	135	7	165	23	
JJ1742 a3	1	65	5.423	1.1	0.189	1.9	27.8	2.4	0.224	2.4	33.1	1.19	7.85	6.8	1159	36	0.76	145	191	8			
Mühlig-Hofmannfjella																							
JJ1700 a1	1	51	2.389	1.1	0.040	2.3	21.8	2.4	0.481	2.4	263.5	12.08	2.26	6.8	1237	84	0.67	114	171	9			
JJ1700 a2	1	60	5.126	1.0	0.052	2.2	15.8	2.4	1.092	2.4	335.1	21.19	2.32	6.8	712	95	0.72	128	179	9			
JJ1700 a3	1	57	1.577	1.1	0.043	2.3	19.4	2.4	0.331	2.4	150.4	7.74	2.61	6.8	1186	55	0.71	91	128	6	158	20	
JJ1700 a4	1	41	0.932	1.1	0.025	2.8	21.1	2.4	0.198	2.4	166.3	7.89	1.52	3.1	1280	60	0.60	91	153	10			
JJ1768 a1	1	38	0.071	2.3	0.008	7.6	11.9	3.3	0.012	3.0	16.6	1.40	0.30	3.8	421	16	0.58	43	74	6			
JJ1768 a2	2	49	0.810	1.2	0.034	2.5	16.5	3.0	0.018	3.0	8.7	0.53	4.04	3.4	1961	19	0.70	93	134	7			
JJ1768 a3	1	41	1.338	1.2	0.040	2.3	20.2	2.8	0.023	2.8	11.9	0.59	3.93	3.8	1989	23	0.76	141	187	8			
JJ1621 a1	1	73	1.429	1.4	0.064	2.1	8.2	3.1	0.017	3.1	2.2	0.27	7.53	6.8	974	9	0.79	91	115	6			
JJ1621 a2	1	73	0.721	1.5	0.034	2.9	4.8	4.3	0.005	4.3	0.8	0.16	9.36	6.8	1327	5	0.79	53	67	4	86	21	
JJ1621 a3	2	64	0.864	1.4	0.042	2.6	6.0	3.0	0.024	3.0	3.4	0.57	9.78	3.8	1383	7	0.74	55	75	8			
Orvinfjella																							
JJ1673 a1	2	76	0.590	1.4	0.060	2.2	6.2	2.5	0.094	2.5	9.7	1.56	2.66	6.8	274	8	0.79	47	59	2			
JJ1673 a2	*1*	*122*	*2.956*	*1.4*	*0.099*	*2.0*	*4.0*	*2.4*	*0.241*	*2.4*	*9.6*	*2.43*	*6.04*	*6.9*	*242*	*6*	*0.87*	*118*	*136*	*4*	*71*	*8*	*Outlier*
JJ1673 a3	1	76	1.538	1.4	0.120	1.9	15.2	2.4	0.237	2.4	30.2	1.98	4.52	6.9	575	22	0.79	59	75	3			
JJ1673 a4	2	64	1.942	1.4	0.159	1.9	18.7	2.4	0.383	2.4	45.0	2.41	3.68	6.9	432	29	0.74	57	77	3			
JJ1720 a1	2	43	2.008	1.8	0.057	2.1	39.3	2.5	0.099	2.5	68.3	1.74	0.82	9.1	564	55	0.62	189	306	19			
JJ1720 a2	*2*	*36*	*1.589*	*1.9*	*0.065*	*3.0*	*58.3*	*3.0*	*0.171*	*3.0*	*154.6*	*2.65*	*0.56*	*2.9*	*502*	*95*	*0.54*	*66*	*122*	*9*	*276*	*21*	*Outlier*
JJ1720 a3	2	58	13.058	1.7	0.275	1.8	66.6	2.4	1.157	2.4	279.7	4.20	3.11	9.1	752	132	0.71	186	260	13			
JJ1720 a5	2	36	1.097	1.1	0.026	3.3	24.9	2.5	0.133	2.5	125.8	5.05	0.69	8.1	650	54	0.54	142	262	19			
JJ1736 a1	2	57	4.949	1.8	0.187	1.8	45.3	2.9	0.018	2.9	4.4	0.10	2.85	9.1	692	46	0.73	188	256	12			
JJ1736 a2	2	57	4.259	1.7	0.157	1.9	41.3	2.7	0.030	2.7	7.9	0.19	2.38	9.1	624	43	0.73	189	258	12	259	3	
JJ1736 a3	2	49	3.094	1.8	0.122	1.9	51.9	3.2	0.122	3.2	4.8	0.09	1.70	8.1	725	53	0.69	182	264	14			
JJ1746 a1	2	68	0.852	2.2	0.030	2.6	6.1	3.1	0.013	3.1	2.6	0.43	3.57	9.0	733	7	0.77	112	146	9			
JJ1746 a2	2	62	0.681	2.3	0.038	2.4	11.1	2.7	0.031	2.7	9.2	0.83	2.35	9.0	693	13	0.75	87	117	6			
JJ1746 a3	2	69	1.244	2.1	0.066	2.0	6.3	3.1	0.014	3.1	1.3	0.21	5.67	9.1	540	7	0.78	88	113	6	141	22	
JJ1746 a5	2	36	0.281	1.5	0.017	4.2	11.1	6.1	0.002	6.1	1.2	0.10	0.91	7.9	591	11	0.58	92	160	12			
JJ1746 a6	*2*	*50*	*0.025*	*1.9*	*0.010*	*6.3*	*3.6*	*35.9*	*0.001*	*35.9*	*0.4*	*0.11*	*1.77*	*7.0*	*662*	*4*	*0.69*	*8*	*12*	*1*			*Outlier*
JJ1746 a7	1	66	1.138	1.7	0.045	2.2	8.3	4.1	0.006	4.1	1.1	0.13	3.14	7.0	570	9	0.77	129	167	8			
JJ1766 a1	0	98	4.990	1.7	0.209	1.8	17.5	2.4	0.317	2.4	26.5	1.52	3.66	9.0	306	24	0.84	130	155	5			
JJ1766 a2	0	111	7.845	1.7	0.349	1.8	41.0	2.4	0.390	2.4	45.9	1.12	2.23	9.1	262	52	0.86	140	162	5	152	10	
JJ1766 a3	0	93	3.119	1.8	0.135	1.9	16.2	2.4	0.282	2.4	33.8	2.09	2.65	9.0	318	24	0.83	115	138	5			

Table A2. *Cont.*

Sample	Term	SR [μm]	He Vol. [ncc]	He 1σ [%]	238U Mass [ng]	238U 1σ [%]	238U Conc. [ppm]	232Th Mass [ng]	232Th 1σ [%]	232Th Conc. [ppm]	Th/U ratio	Sm Mass [ng]	Sm 1σ [%]	Sm Conc. [ppm]	eU [ppm]	Ejec. Corr. (FT)	Uncorr. He-Age [Ma]	FT Corr. He-Age [Ma]	1σ [Ma]	Unweighted Sample Average Age [Ma]	1σ [Ma]	Reason for Exclusion
Orvinfjella																						
JJ1796 a1	2	42	0.055	2.6	0.004	19.4	3.4	0.000	n.c.	0.3	0.10	0.39	4.1	337	4	0.64	63	100	12			
JJ1796 a2	2	56	0.647	1.2	0.061	2.0	19.6	0.012	3.2	3.9	0.20	1.10	3.3	356	21	0.73	73	101	5			
JJ1796 a3	2	40	0.211	1.6	0.024	3.0	24.7	0.006	4.1	6.3	0.26	0.45	3.7	454	26	0.62	59	95	6	99	3	
JJ1797 a1	2	47	0.629	1.2	0.028	2.8	10.8	0.000	n.c.	0.1	0.01	0.46	3.9	179	11	0.67	163	243	14			
JJ1797 a2	2	64	4.087	1.1	0.165	1.8	28.3	0.012	4.1	0.9	0.03	0.90	3.6	154	29	0.76	192	252	10			
JJ1797 a3	1	56	1.238	1.1	0.074	2.0	25.5	0.003	4.6	1.0	0.04	0.49	3.7	167	26	0.73	129	177	8	224	33	
JJ1677 a1	1	71	1.143	1.4	0.101	2.0	12.8	0.325	2.9	41.2	3.22	1.77	7.0	224	22	0.77	49	64	3			
JJ1677 a2	2	42	0.335	1.6	0.039	2.6	10.2	0.026	3.0	6.9	0.67	0.55	7.3	143	12	0.62	55	89	6			
JJ1677 a3	2	50	0.258	1.7	0.044	2.5	8.8	0.029	2.9	5.8	0.66	1.13	7.1	224	10	0.68	35	52	3	68	16	
Wohlthatmassivet																						
JJ1812 a1	1	44	3.504	1.3	0.126	1.9	23.4	0.404	2.4	75.0	3.21	1.29	7.0	240	41	0.63	124	195	11			
JJ1812 a3	2	38	0.551	1.5	0.025	3.7	6.6	0.055	2.6	14.4	2.19	0.43	7.3	114	10	0.58	109	190	13	193	3	
JJ1838 a1	1	51	0.032	3.2	0.018	4.3	12.2	0.004	4.3	2.5	0.20	0.49	3.6	324	13	0.70	11	16	1			
JJ1838 a2	2	73	0.138	1.8	0.007	11.0	5.3	0.037	2.7	26.6	5.06	1.17	3.5	828	12	0.77	44	57	3			
JJ1838 a3	2	70	1.486	1.1	0.160	1.9	26.5	0.021	2.9	3.5	0.13	1.91	3.4	317	27	0.78	68	87	3			
JJ1867 a1	2	41	0.917	1.2	0.077	2.1	13.8	0.032	2.8	5.8	0.42	1.20	7.1	217	15	0.63	80	128	8			
JJ1867 a2	2	44	0.668	1.2	0.062	2.2	12.5	0.024	3.0	4.9	0.39	0.94	6.9	188	14	0.64	73	114	7			
JJ1867 a3	1	64	3.150	1.1	0.180	1.9	21.9	0.087	2.5	10.6	0.48	2.18	7.1	265	24	0.76	118	155	6	132	17	
JJ1886 a1	2	36	0.507	2.3	0.042	3.0	35.3	0.093	3.0	78.0	2.21	1.40	2.7	1172	54	0.55	31	56	4			
JJ1886 a2	2	58	4.155	1.8	0.173	1.8	49.2	0.485	2.4	137.7	2.80	3.87	9.0	1098	82	0.72	107	149	7			
JJ1886 a3	2	40	0.351	2.8	0.031	2.6	27.5	0.055	2.5	49.5	1.80	1.16	9.1	1035	39	0.59	54	91	6			
JJ1931 a1	2	37	0.164	3.3	0.024	3.0	18.7	0.012	10.0	9.1	0.49	0.27	3.3	206	21	0.58	22	37	3			
JJ1931 a2	1	50	0.664	2.2	0.078	2.0	23.1	0.045	2.6	13.4	0.58	0.90	9.1	266	26	0.70	57	82	4			
JJ1931 a3	2	41	0.316	2.6	0.045	3.0	20.2	0.023	3.0	10.1	0.50	0.44	2.9	195	23	0.62	22	36	2			
JJ1931 a4	2	53	0.569	2.5	0.067	2.0	18.8	0.040	2.6	11.2	0.59	0.68	3.0	192	21	0.71	57	81	4			
JJ1931 a5	1	49	0.712	1.8	0.071	2.2	26.5	0.033	2.7	12.2	0.46	0.67	8.2	251	29	0.68	70	102	6			
JJ1886 a5	1	38	4.468	1.6	0.230	1.8	166.9	0.399	2.4	289.9	1.74	2.03	7.8	1477	235	0.59	108	184	12			
JJ1875 a1	1	46	15.214	1.7	0.832	2.5	405.2	6.845	2.0	3332.8	8.22	7.62	2.7	3712	1188	0.64	35	54	3			
JJ1875 a2	2	34	7.250	1.7	0.330	1.8	322.9	2.909	2.4	2849.8	8.83	3.82	10.1	3744	993	0.50	57	114	9			
JJ1875 a3	1	45	10.037	1.7	0.404	1.8	370.0	4.154	2.4	3803.4	10.28	4.91	10.1	4495	1264	0.63	58	92	6	86	19	
JJ1875 a4	1	38	3.681	1.8	0.144	3.0	245.9	1.335	2.0	2273.4	9.24	2.50	4.2	4262	780	0.57	45	79	5			
JJ1875 a5	0	56	16.189	1.6	0.722	1.8	652.5	5.455	2.4	4931.6	7.56	4.86	7.8	4392	1811	0.71	65	92	5			
JJ1890 a1	2	42	0.366	2.6	0.021	3.0	10.7	0.067	3.0	34.3	3.20	0.33	3.3	169	19	0.61	44	72	5			*Outlier*
JJ1890 a2	2	55	0.457	2.5	0.017	3.8	6.2	0.065	2.5	24.0	3.87	0.48	9.2	177	12	0.70	104	148	8			
JJ1890 a3	2	67	1.000	2.1	0.034	2.5	11.7	0.098	2.5	33.9	2.90	0.50	9.2	171	20	0.74	134	181	9			*Outlier*
JJ1890 a4	0	88	0.623	2.5	0.018	3.8	6.9	0.092	2.5	35.7	5.17	0.42	3.0	163	15	0.82	119	146	6	146	1	
JJ1890 a5	0	95	2.198	1.6	0.076	2.1	20.3	0.282	2.4	74.7	3.69	0.79	7.9	209	38	0.83	121	145	5			

Table A2. *Cont.*

Sample	Term	SR [µm]	He		^{238}U			^{232}Th			Th/U ratio	Sm			eU [ppm]	Ejec. Corr. (F$_T$)	Uncorr. He-Age [Ma]	F$_T$ Corr. He-Age [Ma]	1σ [Ma]	Unweighted Sample Average Age [Ma]	1σ [Ma]	Reason for Exclusion
			Vol. [ncc]	1σ [%]	Mass [ng]	1σ [%]	Conc. [ppm]	Mass [ng]	1σ [%]	Conc. [ppm]		Mass [ng]	1σ [%]	Conc. [ppm]								
JJ1897 a1	2	106	8.254	1.7	0.339	1.8	27.2	0.847	2.4	67.9	2.50	2.39	10.1	192	43	0.85	121	142	4			
JJ1897 a2	0	91	3.277	1.8	0.151	1.9	25.3	0.425	2.4	71.4	2.82	1.09	10.2	183	42	0.83	103	125	4			
JJ1897 a3	*1*	*64*	*0.950*	*2.1*	*0.050*	*3.0*	*12.8*	*0.111*	*3.0*	*28.2*	*2.21*	*0.82*	*2.8*	*210*	*19*	*0.75*	*51*	*68*	*3*			*Outlier*
JJ1897 a4	1	80	2.847	1.8	0.122	1.9	17.5	0.300	2.4	43.2	2.46	1.13	2.9	163	28	0.80	116	144	5	134	9	
JJ1897 a5	1	78	2.734	1.6	0.136	1.9	20.9	0.329	2.4	50.4	2.41	1.21	7.9	186	33	0.80	100	126	5			
Wohlthatmassivet																						
JJ1911 a1	1	72	8.502	1.7	0.675	1.8	107.7	0.707	2.4	112.8	1.05	1.32	10.1	211	134	0.79	82	104	4	109	3	
JJ1911 a2	0	71	3.828	1.8	0.285	1.8	188.8	0.331	2.4	219.0	1.16	0.45	10.2	296	240	0.78	86	109	4			
JJ1911 a3	2	67	7.080	1.7	0.375	1.8	64.4	1.230	2.4	211.3	3.28	1.71	10.1	295	114	0.76	86	113	5			
JJ1924 a1	0	53	1.528	1.9	0.069	3.0	29.2	0.008	12.0	3.5	0.12	0.32	2.9	136	30	0.72	74	104	6			
JJ1924 a2	1	69	4.386	1.7	0.228	1.8	28.9	0.024	2.8	3.1	0.11	0.87	9.1	111	30	0.78	149	192	8			
JJ1924 a3	2	41	0.872	2.1	0.036	2.4	14.0	0.002	5.5	0.8	0.06	0.20	9.4	79	14	0.63	187	298	19			
JJ1924 a4	2	32	1.919	2.0	0.098	3.0	109.2	0.010	4.0	11.5	0.11	0.23	4.8	260	112	0.52	66	127	10			
JJ1924 a5	1	64	5.332	1.6	0.177	1.9	41.0	0.014	3.2	3.1	0.08	1.06	8.0	246	42	0.76	229	301	13			
JJ1924 a6	2	46	7.020	1.6	0.271	1.8	113.0	0.019	3.0	7.8	0.07	0.72	7.4	298	115	0.67	203	304	17			
JJ1940 a1	2	47	4.496	1.3	0.233	1.8	50.9	1.253	2.4	273.7	5.37	5.02	6.9	1096	115	0.64	65	102	6			
JJ1940 a2	2	31	0.901	1.4	0.064	2.2	24.0	0.362	2.4	136.7	5.69	1.16	6.8	438	56	0.46	47	102	9	110	12	
JJ1940 a3	1	34	1.093	1.4	0.057	2.2	20.3	0.300	2.4	106.6	5.25	1.06	7.0	377	45	0.52	66	128	10			
SG-25 a1	1	48	0.724	1.0	0.044	2.3	28.7	0.099	2.5	64.9	2.26	0.37	4.9	246	44	0.67	85	128	7			
SG-25 a2	1	46	0.450	1.2	0.026	2.9	23.9	0.057	2.6	51.7	2.17	0.22	4.8	201	36	0.65	89	137	8			
SG-25 a3	*0*	*57*	*0.602*	*1.0*	*0.045*	*2.2*	*35.1*	*0.091*	*2.5*	*70.8*	*2.01*	*0.29*	*4.7*	*224*	*52*	*0.73*	*72*	*98*	*4*			*Outlier*
SG-25 a4	1	53	1.246	1.7	0.075	2.0	18.9	0.162	2.5	40.9	2.16	0.76	5.0	192	29	0.70	86	123	6	133	9	
SG-25 a5	0	48	0.484	1.8	0.029	2.6	20.5	0.060	2.5	42.8	2.09	0.28	5.0	197	31	0.68	88	129	7			
SG-25 a6	1	46	0.972	1.7	0.055	2.1	28.8	0.101	2.5	53.3	1.85	0.47	5.1	247	41	0.65	97	149	9			
SG-28 a1	2	63	0.436	1.8	0.021	3.1	11.4	0.024	3.1	12.7	1.12	0.49	7.4	264	14	0.75	116	155	8			
SG-28 a2	*1*	*46*	*0.135*	*2.2*	*0.004*	*34.6*	*9.8*	*0.003*	*5.5*	*7.4*	*0.76*	*0.08*	*9.3*	*249*	*11*	*0.66*	*218*	*329*	*81*			*Large error*
SG-28 a3	*2*	*55*	*0.472*	*1.8*	*0.016*	*4.7*	*13.4*	*0.014*	*3.8*	*11.8*	*0.88*	*0.28*	*7.7*	*232*	*16*	*0.71*	*180*	*252*	*15*			*Outlier*
SG-28 a4	1	67	0.393	1.5	0.019	4.7	3.6	0.014	3.8	2.7	0.77	0.28	7.7	201	4	0.77	101	132	7	144	9	
SG-28 a5	*2*	*44*	*0.726*	*1.5*	*0.015*	*5.5*	*4.4*	*0.017*	*3.2*	*4.9*	*1.11*	*0.45*	*7.1*	*132*	*6*	*0.65*	*259*	*401*	*27*			*Older than FT.He-implantation?*
SG-28 a6	2	45	0.159	1.9	0.008	10.0	2.5	0.009	3.3	2.8	1.15	0.47	7.4	143	3	0.65	93	144	12			
Continental wedge																						
JJ1730 a1	*2*	*35*	*0.023*	*3.9*	*0.002*	*66.2*	*0.6*	*0.007*	*3.2*	*2.2*	*3.92*	*0.10*	*7.3*	*29*	*1*	*0.53*	*43*	*81*	*23*			*Large error*
JJ1730 a2	1	58	0.538	1.3	0.043	2.5	7.0	0.052	2.7	8.5	1.21	0.42	7.0	70	9	0.73	76	104	5	95	10	
JJ1730 a3	2	47	0.146	1.8	0.010	9.8	2.1	0.029	2.9	6.2	2.91	0.21	7.2	45	4	0.65	65	100	8			
JJ1731 a1	0	93	0.969	2.2	0.046	2.2	7.9	0.179	2.4	30.7	3.88	0.49	9.2	85	15	0.83	86	104	4			
JJ1731 a2	2	66	0.926	2.1	0.046	2.2	7.8	0.157	2.5	26.5	3.38	0.48	9.2	81	14	0.76	87	115	5	105	8	
JJ1731 a3	0	74	0.735	2.2	0.042	2.3	7.3	0.142	2.5	24.5	3.36	0.48	9.2	82	13	0.79	76	97	4			

Table A2. *Cont.*

Sample	Term	SR [μm]	He Vol. [ncc]	He 1σ [%]	238U Mass [ng]	238U 1σ [%]	238U Conc. [ppm]	232Th Mass [ng]	232Th 1σ [%]	232Th Conc. [ppm]	Th/U ratio	Sm Mass [ng]	Sm 1σ [%]	Sm Conc. [ppm]	eU [ppm]	Ejec. Corr. (FT)	Uncorr. He-Age [Ma]	FT Corr. He-Age Age [Ma]	FT Corr. He-Age 1σ [Ma]	Unw. Sample Average Age [Ma]	Unw. Sample Average 1σ [Ma]	Reason for Exclusion
										Continental wedge												
JJ1974 a1	1	65	0.076	5.4	0.002	41.9	0.4	0.001	9.6	0.2	0.57	2.08	10.1	535	0	0.76	33	44	5			
JJ1974 a3	1	42	0.031	7.6	0.000	n.c.	0.0	0.000	n.c	0.0	0.00	0.72	10.2	332	0	0.64	43	66	12			
JJ1974 a6	0	61	0.062	2.5	0.000	n.c.	0.1	0.000	n.c	0.1	0.86	0.73	4.9	389	0	0.77	82	106	14	70	23	
JJ1974 a7	1	48	0.048	2.8	0.000	n.c.	0.1	0.000	n.c	0.1	0.73	1.08	7.0	245	0	0.69	43	63	9			
JJ1974 a8	1	61	0.671	1.4	0.009	9.8	1.8	0.000	n.c	0.0	0.00	1.52	7.0	306	2	0.75	256	341	24			Outlier
JJ1976 a1	2	53	0.451	2.4	0.017	3.8	4.8	0.141	2.5	39.4	8.21	2.77	9.0	777	14	0.69	51	74	5			
JJ1976 a2	2	46	0.423	2.4	0.025	3.0	9.5	0.092	3.0	34.5	3.62	1.85	2.7	690	18	0.64	36	56	3	69	8	
JJ1976 a3	0	56	0.206	3.0	0.007	8.2	5.5	0.075	2.5	55.3	10.08	0.99	9.1	732	18	0.71	51	72	4			
JJ1976 a4	0	46	0.187	3.6	0.011	5.5	9.4	0.057	2.5	47.9	5.12	0.89	3.4	748	21	0.65	49	75	5			
JJ1984 a1	2	42	0.408	1.5	0.037	2.8	9.6	0.065	2.6	17.2	1.78	2.35	7.1	621	14	0.62	47	76	5			
JJ1984 a2	2	42	0.049	2.8	0.006	11.4	1.9	0.000	n.c	0.1	0.06	1.30	6.8	382	2	0.63	23	37	3			
JJ1984 a3	1	89	0.856	1.4	0.076	2.1	6.9	0.050	2.7	4.6	0.67	11.61	6.8	1057	8	0.83	39	47	2	57	16	
JJ1984 a4	1	65	1.080	1.4	0.108	1.9	16.7	0.011	3.3	1.8	0.11	6.86	6.8	1065	17	0.76	53	70	3			
S25-1 a1	2	36	0.146	3.6	0.009	6.8	7.4	0.056	2.5	45.9	6.24	0.43	9.1	353	18	0.53	47	88	7			
S25-1 a2	2	35	0.179	3.4	0.012	5.2	8.5	0.067	2.5	48.4	5.70	0.45	9.1	326	20	0.53	47	90	7			
S25-1 a3	2	46	0.116	3.9	0.015	4.0	7.0	0.023	3.0	10.5	1.50	0.70	3.0	321	9	0.65	20	31	2	83	7	Outlier
S25-1 a4	2	44	0.238	3.3	0.016	3.9	10.2	0.078	2.5	49.0	4.81	0.69	3.6	434	22	0.68	49	72	4			
S25-1 a5	2	45	0.351	2.0	0.028	3.0	13.0	0.084	2.5	39.6	3.04	1.01	7.9	475	22	0.64	52	80	5			
S30-1 a1	2	48	0.271	2.9	0.035	3.0	10.8	0.012	10.0	3.8	0.35	1.53	2.8	478	12	0.68	23	34	2			Outlier
S30-1 a2	2	53	0.193	3.1	0.023	3.1	4.8	0.002	5.3	0.5	0.11	1.10	9.1	236	5	0.71	49	70	4			
S30-1 a5	1	65	0.674	1.8	0.070	2.0	14.4	0.004	4.7	0.8	0.06	2.94	7.8	600	15	0.76	58	76	4	72	4	
S30-1 a6	2	48	0.197	2.3	0.025	3.2	7.1	0.002	5.6	0.7	0.09	1.37	7.9	393	7	0.68	44	65	4			
S30-1 a7	1	61	0.334	1.9	0.036	2.6	12.2	0.017	3.0	5.8	0.48	1.11	7.9	377	14	0.75	56	75	4			
S30-1 z1	2	47	20.810	1.6	0.616	1.8	132.0	0.185	2.4	40.0	0.30	0.02	13.3	4	141	0.74	256	344	15			
S30-1 z2	2	55	40.120	1.6	1.076	1.8	158.0	0.400	2.4	59.0	0.37	0.04	10.4	6	172	0.78	277	358	15	348	7	
S30-1 z3	2	50	22.540	1.6	0.660	1.8	122.0	0.188	2.4	35.0	0.28	0.02	14.6	3	130	0.76	259	342	15			
J02.02/2 z1	2	54	50.110	1.6	1.156	1.8	190.5	0.267	2.4	44.1	0.23	0.03	11.7	4	201	0.77	331	429	18			
J02.02/2 z2	2	51	46.337	1.6	1.289	1.8	207.4	0.323	2.4	52.0	0.25	0.03	11.6	5	220	0.76	274	361	15	389	29	
J02.02/2 z3	2	48	67.248	1.6	1.828	1.8	322.4	0.409	2.4	72.2	0.22	0.05	9.8	8	339	0.75	282	377	17			
J03.02/1 a1	1	49	0.095	2.4	0.011	5.5	5.6	0.000	n.c.	0.1	0.02	0.23	4.1	115	6	0.69	59	86	6			
J03.02/1 a2	1	45	0.112	2.3	0.012	5.0	5.6	0.001	17.0	0.6	0.10	0.69	3.5	310	6	0.66	50	75	5	83	5	
J03.02/1 a4	1	49	0.307	2.3	0.010	5.9	4.9	0.000	n.c.	0.2	0.04	0.52	5.1	249	5	0.69	172	250	17			Outlier
J03.02/1 a5	2	62	0.357	1.8	0.037	2.4	6.2	0.008	3.5	1.4	0.22	0.68	5.0	112	7	0.75	65	87	4			

Table footnote: Term: Number of crystal terminations. SR: Sphere radius. Amount of helium is given in nano-cubic-cm at standard temperature and pressure. Amounts of radioactive elements are given in nanograms. Ejection correction (F$_T$): correction factor for alpha-ejection (according to Farley et al. [84] and Hourigan et al. [85]). Uncertainties of helium and the radioactive element contents are given as 1σ in relative error %. When radioactive element concentrations were close to, or below, the detection limit, uncertainties were not calculated (n.c.). Uncertainty of the single-grain age is given as 1σ in Ma and it includes both the analytical uncertainty and the estimated uncertainty of the F$_T$. Uncertainty of the sample average age is 1σ in Ma.

Appendix C

Table A3. Comparison between the three modelling scenarios tested.

Sample	Locality	Elev. [m]	Model 1		Model 2		Model 3		*Jurassic Reheating?*
			Good	*Acc.*	*Good*	*Acc.*	*Good*	*Acc.*	
	Mühlig-Hofmannfjella								
JJ1742	Mühlig-Hofmannfjella	1410	*0*	*0*	**40**	**255**	15	121	No
	Orvinfjella								
JJ1700	Drygalskifjella	1745	*0*	*9*	238	721	**496**	**1192**	No
JJ1768	Drygalskifjella	2145	34	123	141	567	**166**	**785**	No
JJ1673	Conradfjella	1200	*0*	*0*	0	41	0	6	No
JJ1720	Conradfjella	2985	*0*	*33*	49	272	**293**	**1092**	Limited (<30 °C)
JJ1736	Conradfjella	2605	88	1007	55	497	**164**	**1047**	No
JJ1746	Conradfjella	1590	*0*	*0*	0	242	**8**	**348**	No
JJ1766	Gjeruldsenhøgda	2100	*0*	*0*	0	186	0	160	Limited (<30 °C)
JJ1796	Dallmannfjellet	1745	2	5	**3**	**61**	1	14	Limited (<30 °C)
JJ1797	Dallmannfjellet	1745	3	1	**6**	**97**	3	15	Limited (<30 °C)
JJ1677	Henriksenskjera	1315	*0*	*8*	**112**	**744**	37	276	No
	Wohlthatmassivet								
JJ1812	Zwieselhøgda	2965	**0**	**311**	0	205	*0*	*84*	Yes
JJ1867	Petermannkjedene	1410	23	217	31	363	11	265	Yes*
JJ1886	Petermannkjedene	1125	*0*	*0*	69	886	**126**	**2146**	Yes*
JJ1931	Petermannkjedene	1475	*0*	*0*	44	179	**127**	**438**	Yes*
JJ1875	Madsensåta	1400	*154*	*975*	222	1297	**367**	**1655**	Yes*
JJ1890	Gruberfjella	2800	0	658	**0**	**789**	*0*	*209*	Limited (<20 °C)
JJ1897	Gruberfjella	2175	*0*	*0*	**147**	**418**	70	204	Limited (<20 °C)
JJ1911	Gruberfjella	1285	*0*	*0*	**0**	**74**	0	70	Yes*
JJ1924	Weyprechtfjella	2685	**151**	**775**	91	498	*56*	*353*	No
JJ1940	Oddenskjera	1190	*0*	*0*	**0**	**58**	0	37	Yes*
SG-25	E. Wohlthatmassivet	1795	*0*	*2*	**47**	**193**	9	20	Limited (<20 °C)
	Continental wedge								
JJ1730	Sigurdsvodene	1035	*4*	*83*	7	155	**13**	**197**	No
JJ1731	Sigurdsvodene	1155	*0*	*0*	0	193	**0**	**285**	Yes*
JJ1976	Starheimtind	1345	*0*	*0*	**0**	**79**	0	37	Yes*
JJ1984	Schirmacheroasen	50	*0*	*0*	**6**	**125**	1	38	No
S25.1	Schirmacheroasen	150	0	191	**0**	**302**	*0*	*168*	Yes*
S30.1	Schirmacheroasen	150	*0*	*0*	**4**	**64**	1	18	No
J03.02./1	Schirmacheroasen	150	*0*	*0*	**0**	**59**	0	0	No

Table footnote: Model 1: Only monotonic cooling. Model 2: Late Paleozoic peneplanation and late Paleozoic—early Mesozoic reburial. Model 3: Late Paleozoic peneplanation and late Paleozoic—early Mesozoic reburial, followed by Late Triassic—Early Jurassic cooling and reburial. Note that samples were not forced to higher temperatures in the Jurassic, merely given the possibility to reheat. Many samples do not show Jurassic reheating when modelled with these constraints. The results are summarized in the column 'Jurassic reheating?': No—samples showed no Jurassic reheating; Limited—samples showed minor Jurassic reheating (temperature indicated); Yes—sample showed Jurassic reheating; Yes*—While these samples are compatible with the constraints used in Model 3 and show Jurassic reheating when modelled with these constraints, their AFT and AHe ages are too young to actually constrain the thermal histories in the Jurassic. The *t*–*T* paths are thus only determined by the constraint boxes; the data cannot be used to either reject or support Jurassic reheating.

References

1. Jacobs, J.; Bauer, W.; Fanning, C.M. New age constraints for Grenville-age metamorphism in western central Dronning Maud Land (East Antarctica), and implications for the palaeogeography of Kalahari in Rodinia. *Int. J. Earth Sci.* **2003**, *92*, 301–315. [CrossRef]
2. Jacobs, J.; Bauer, W.; Fanning, C.M. Late Neoproterozoic/Early Palaeozoic events in central Dronning Maud Land and significance for the southern extension of the East African Orogen into East Antarctica. *Precambrian Res.* **2003**, *126*, 27–53. [CrossRef]
3. Storey, B.; Kyle, P. An active mantle mechanism for Gondwana breakup. *S. Afr. J. Geol.* **1997**, *100*, 283–290.
4. König, M.; Jokat, W. Advanced insights into magmatism and volcanism of the Mozambique Ridge and Mozambique Basin in the view of new potential field data. *Geophys. J. Int.* **2010**, *180*, 158–180. [CrossRef]
5. Boger, S.D. Antarctica—Before and after Gondwana. *Gondwana Res.* **2011**, *19*, 335–371. [CrossRef]

6. Slater, B.J.; McLoughlin, S.; Hilton, J. A high-latitude Gondwanan lagerstätte: The Permian permineralised peat biota of the Prince Charles Mountains, Antarctica. *Gondwana Res.* **2015**, *27*, 1446–1473. [CrossRef]

7. Stone, P. Geology reviewed for the Falkland Islands and their offshore sedimentary basins, South Atlantic Ocean. *Earth Environ. Sci. Trans. R. Soc. Edinb.* **2016**, *106*, 115–143. [CrossRef]

8. Meier, S. Paleozoic and Mesozoic Tectono-Thermal History of Central Dronning Maud Land, East Antarctica—Evidence From Fission-Track Thermochronology. Ph.D. Thesis, University of Bremen, Bremen, Germany, 1999.

9. Meier, S.; Jacobs, J.; Olesch, M. Tectono-thermal Evolution of Central Dronning Maud Land, East Antarctica, from Mid-Palaeozoic to Cenozoic Times: Zircon and Apatite Fission-Track Data from the Conradgebirge and Östliche Petermannkette. *Geol. Jahrb. Reihe B* **2004**, *96*, 423–448.

10. Emmel, B.; Jacobs, J.; Crowhurst, P.; Daszinnies, M.C. Combined apatite fission-track and single grain apatite (U–Th)/He ages from basement rocks of central Dronning Maud Land (East Antarctica)—Possible identification of thermally overprinted crustal segments? *Earth Planet. Sci. Lett.* **2007**, *264*, 72–88. [CrossRef]

11. Jacobs, J.; Lisker, F. Post Permian tectono-thermal evolution of western Dronning Maud Land, East Antarctica: An apatite fission-track approach. *Antarct. Sci.* **1999**, *11*, 451–460. [CrossRef]

12. Emmel, B.; Jacobs, J.; Daszinnies, M.C. Combined Titanite and Apatite Fission-Track Data from Gjelsvikfjella, East Antarctica—Another Piece of A Concealed Intracontinental Permo-Triassic Gondwana Rift Basin? *Geol. Soc.* **2009**, *324*, 317–330. [CrossRef]

13. Krohne, N. From Active to Passive Margins: The Basin and Highland Evolution of the Weddell Sea Sector, East Antarctica. Ph.D. Thesis, University of Bremen, Bremen, Germany, 2017.

14. Sirevaag, H.; Jacobs, J.; Ksienzyk, A.K.; Dunkl, I.; Marschall, H.R. Extent, thickness and erosion of the Jurassic continental flood basalts of Dronning Maud Land, East Antarctica: A low-T thermochronological approach. *Gondwana Res.* **2018**, *61*, 222–243. [CrossRef]

15. Jacobs, J.; Elburg, M.; Läufer, A.; Kleinhanns, I.C.; Henjes-Kunst, F.; Estrada, S.; Ruppel, A.S.; Damaske, D.; Montero, P.; Bea, F. Two distinct Late Mesoproterozoic/Early Neoproterozoic basement provinces in central/eastern Dronning Maud Land, East Antarctica: The missing link, 15–21 °E. *Precambrian Res.* **2015**, *265*, 249–272. [CrossRef]

16. Smith, A.G.; Hallam, A. The Fit of the Southern Continents. *Nature* **1970**, *225*, 139–144. [CrossRef]

17. Martin, A.K.; Hartnady, C.J. Plate tectonic development of the South West Indian Ocean: A revised reconstruction of East Antarctica and Africa. *J. Geophys. Res.* **1986**, *91*, 4767–4786. [CrossRef]

18. Groenewald, P.B.; Grantham, G.H.; Watkeys, M.K. Geological evidence for a Proterozoic to Mesozoic link between southeastern Africa and Dronning Maud Land, Antarctica. *J. Geol. Soc.* **1991**, *148*, 1115–1123. [CrossRef]

19. Moyes, A.B.; Barton, J.M.; Groenewald, P.B. Late Proterozoic to Early Palaeozoic tectonism in Dronning Maud Land, Antarctica: Supercontinental fragmentation and amalgamation. *J. Geol. Soc.* **1993**, *150*, 833–842. [CrossRef]

20. Groenewald, P.B.; Moyes, A.B.; Grantham, G.H.; Krynauw, J.R. East Antarctic crustal evolution: Geological constraints and modelling in western Dronning Maud Land. *Precambrian Res.* **1995**, *75*, 231–250. [CrossRef]

21. König, M.; Jokat, W. The Mesozoic breakup of the Weddell Sea. *J. Geophys. Res Solid Earth* **2006**, *111*, B12102. [CrossRef]

22. Jacobs, J.; Fanning, C.M.; Henjes-Kunst, F.; Olesch, M.; Paech, H.J. Continuation of the Mozambique Belt into East Antarctica: Grenville-Age Metamorphism and Polyphase Pan-African High-Grade Events in Central Dronning Maud Land. *J. Geol.* **1998**, *106*, 385–406. [CrossRef]

23. Jacobs, J.; Pisarevsky, S.; Thomas, R.J.; Becker, T. The Kalahari Craton during the assembly and dispersal of Rodinia. *Precambrian Res.* **2008**, *160*, 142–158. [CrossRef]

24. Leinweber, V.T.; Jokat, W. The Jurassic history of the Africa–Antarctica corridor—New constraints from magnetic data on the conjugate continental margins. *Tectonophysics* **2012**, *530*, 87–101. [CrossRef]

25. Arndt, N.T.; Todt, W.; Chauvel, C.; Tapfer, M.; Weber, K. U-Pb zircon age and Nd isotopic composition of granitoids, charnockites and supracrustal rocks from Heimefrontfjella, Antarctica. *Geol. Rundsch.* **1991**, *80*, 759–777. [CrossRef]

26. Thomas, R.J.; Agenbacht, A.L.; Cornell, D.H.; Moore, J.M. The Kibaran of southern Africa: Tectonic evolution and metallogeny. *Ore Geol. Rev.* **1994**, *9*, 131–160. [CrossRef]

27. Wareham, C.D.; Pankhurst, R.J.; Thomas, R.J.; Storey, B.C.; Grantham, G.H.; Jacobs, J.; Eglington, B.M. Pb, Nd, and Sr Isotope Mapping of Grenville-Age Crustal Provinces in Rodinia. *J. Geol.* **1998**, *106*, 647–660. [CrossRef]

28. Jacobs, J.; Thomas, R.J.; Weber, K. Accretion and indentation tectonics at the southern edge of the Kaapvaal craton during the Kibaran (Grenville) orogeny. *Geology* **1993**, *21*, 203–206. [CrossRef]

29. Jacobs, J.; Klemd, R.; Fanning, C.M.; Bauer, W.; Colombo, F. Extensional Collapse of the Late Neoproterozoic-Early Palaeozoic East African-Antarctic Orogen in Central Dronning Maud Land, East Antarctica. *Geol. Soc.* **2003**, *206*, 271–287. [CrossRef]

30. Jacobs, J.; Bingen, B.; Thomas, R.J.; Bauer, W.; Wingate, M.T.; Feitio, P. Early Palaeozoic orogenic Collapse and Voluminous Late-Tectonic Magmatism in Dronning Maud Land and Mozambique: Insights into the Partially Delaminated Orogenic Root of the East African–Antarctic Orogen? *Geol. Soc.* **2008**, *308*, 69–90. [CrossRef]

31. Jacobs, J.; Thomas, R.J. Himalayan-type indenter-escape tectonics model for the southern part of the late Neoproterozoic–early Paleozoic East African–Antarctic orogen. *Geology* **2004**, *32*, 721–724. [CrossRef]

32. Jacobs, J.; Ahrendt, H.; Kreutzer, H.; Weber, K. K-Ar, ^{40}Ar-^{39}Ar and apatite fission-track evidence for Neoproterozoic and Mesozoic basement rejuvenation events in the Heimefrontfjella and Mannefallknausane (East Antarctica). *Precambrian Res.* **1995**, *75*, 251–262.

33. Golynsky, A.; Jacobs, J. Grenville-Age versus Pan-African magnetic anomaly imprints in Western Dronning Maud Land, East Antarctica. *J. Geol.* **2001**, *109*, 136–142. [CrossRef]

34. Bauer, W.; Siemes, H.; Spaeth, G.; Jacobs, J. Transpression and tectonic exhumation in the Heimefrontfjella, western orogenic front of the East African/Antarctic Orogen, revealed by quartz textures of high strain domains. *Pol. Res.* **2016**, *35*, 25420. [CrossRef]

35. Ruppel, A.; Jacobs, J.; Eagles, G.; Läufer, A.; Jokat, W. New geophysical data from a key region in East Antarctica: Estimates for the spatial extent of the Tonian Oceanic Arc Super Terrane (TOAST). *Gondwana Res.* **2018**, *59*, 97–107. [CrossRef]

36. Jacobs, J.; Opås, B.; Elburg, M.A.; Läufer, A.; Estrada, S.; Ksienzyk, A.K.; Damaske, D.; Hofmann, M. Cryptic sub-ice geology revealed by a U-Pb zircon study of glacial till in Dronning Maud Land, East Antarctica. *Precambrian Res.* **2017**, *294*, 1–14. [CrossRef]

37. Dalziel, I.W.; Lawver, L.A.; Norton, I.O.; Gahagan, L.M. The Scotia Arc: Genesis, Evolution, Global Significance. *Annu. Rev. Earth Planet. Sci.* **2013**, *41*, 767–793. [CrossRef]

38. Plumstead, E.P. *A New Assemblage of Plant Fossils from Milorgfjella, Dronning Maud Land*; British Antarctic Survey: Cambridge, UK, 1975; Volume 83.

39. Olaussen, S. Sedimentological research in northwestern part of Dronning Maud Land. *Rep. Norwegian Antarct. Res. Expedition* **1985**, *22*, 75–88.

40. Lindström, S. Early Late Permian palynostratigraphy and palaeo-biogeography of Vestfjella, Dronning Maud Land, Antarctica. *Rev. Palaeobot. Palynol.* **1995**, *86*, 157–173. [CrossRef]

41. Lindström, S. Early Permian palynostratigraphy of the northern Heimefrontfjella mountain-range, Dronning Maud Land, Antarctica. *Rev. Palaeobot. Palynol.* **1995**, *89*, 359–415. [CrossRef]

42. Bauer, W. Permian sedimentary cover, Heimefrontfjella, western Dronning Maud Land (East Antarctica). *Polarforschung* **2009**, *79*, 39–42.

43. McKelvey, B.C.; Webb, P.N.; Kohn, B.P. Stratigraphy of the Taylor and lower Victoria Groups (Beacon Supergroup) between the Mackay Glacier and Boomerang Range, Antarctica. *N. Z. J. Geol. Geophys.* **1977**, *20*, 813–863. [CrossRef]

44. Barrett, P.J. History of the Ross Sea region during the deposition of the Beacon Supergroup 400–180 million years ago. *J. R. Soc. N. Z.* **1981**, *11*, 447–458. [CrossRef]

45. Isbell, J.L. The Kukri Erosion Surface; a reassessment of its relationship to rocks of the Beacon Supergroup in the central Transantarctic Mountains, Antarctica. *Antarct. Sci.* **1999**, *11*, 228–238. [CrossRef]

46. Johnson, M.R. Stratigraphy and Sedimentology of the Cape and Karoo Sequences in the Eastern Cape Province. Ph.D. Thesis, Rhodes University, Grahamstown, South Africa, 1976.

47. Näslund, J.O. Landscape development in western and central Dronning Maud Land, East Antarctica. *Antarct. Sci.* **2001**, *13*, 302–311. [CrossRef]

48. Matsuoka, N.; Thomachot, C.E.; Oguchi, C.T.; Hatta, T.; Abe, M.; Matsuzaki, H. Quaternary bedrock erosion and landscape evolution in the Sør Rondane Mountains, East Antarctica: Reevaluating rates and processes. *Geomorphology* **2006**, *81*, 408–420. [CrossRef]

49. Suganuma, Y.; Miura, H.; Zondervan, A.; Okuno, J.I. East Antarctic deglaciation and the link to global cooling during the Quaternary: Evidence from glacial geomorphology and 10Be surface exposure dating of the Sør Rondane Mountains, Dronning Maud Land. *Quatern. Sci. Rev.* **2014**, *97*, 102–120. [CrossRef]

50. Duncan, R.A.; Hooper, P.R.; Rehacek, J.; Marsh, J.S.; Duncan, A.R. The timing and duration of the Karoo igneous event, southern Gondwana. *J. Geophys. Res. Solid Earth* **1997**, *102*, 18127–18138. [CrossRef]

51. Luttinen, A.V.; Furnes, H. Flood basalts of vestfjella: Jurassic magmatism across an Archaean–Proterozoic lithospheric boundary in Dronning Maud Land, Antarctica. *J. Petrol.* **2000**, *41*, 1271–1305. [CrossRef]

52. Riley, T.R.; Knight, K.B. Age of Pre-Break-Up Gondwana Magmatism. *Antarct. Sci.* **2001**, *13*, 99–110. [CrossRef]

53. Jourdan, F.; Féraud, G.; Bertrand, H.; Watkeys, M.K.; Renne, P.R. Distinct brief major events in the Karoo large igneous province clarified by new ^{40}Ar/^{39}Ar ages on the Lesotho basalts. *Lithos* **2007**, *98*, 195–209. [CrossRef]

54. Svensen, H.; Corfu, F.; Polteau, S.; Hammer, Ø.; Planke, S. Rapid magma emplacement in the Karoo Large Igneous Province. *Earth Planet. Sci. Lett.* **2012**, *325*, 1–9. [CrossRef]

55. Cleverly, R.W.; Bristow, J.W. Revised volcanic stratigraphy of the Lebombo Monocline. *Trans. Geol. Soc. S. Afr.* **1979**, *82*, 227–230.

56. Furnes, H.; Vad, E.; Austrheim, H.; Mitchell, J.G.; Garmann, L.B. Geochemistry of basalt lavas from Vestfjella and adjacent areas, Dronning Maud Land, Antarctica. *Lithos* **1987**, *20*, 337–356. [CrossRef]

57. Harris, C.; Marsh, J.S.; Duncan, A.R.; Erlank, A.J. The Petrogenesis of the Kirwan Basalts of Dronning Maud Land, Antarctica. *J. Petrol.* **1990**, *31*, 341–369. [CrossRef]

58. Riley, T.R.; Millar, I.L.; Watkeys, M.K.; Curtis, M.L.; Leat, P.T.; Klausen, M.B.; Fanning, C.M. U–Pb zircon (SHRIMP) ages for the Lebombo rhyolites, South Africa: Refining the duration of Karoo volcanism. *J. Geol. Soc.* **2004**, *161*, 547–550. [CrossRef]

59. Luttinen, A.V.; Heinonen, J.S.; Kurhila, M.; Jourdan, F.; Mänttäri, I.; Vuori, S.K.; Huhma, H. Depleted Mantle-sourced CFB Magmatism in the Jurassic Africa–Antarctica Rift: Petrology and ^{40}Ar/^{39}Ar and U/Pb Chronology of the Vestfjella Dyke Swarm, Dronning Maud Land, Antarctica. *J. Petrol.* **2015**, *56*, 919–952. [CrossRef]

60. Rolf, C.; Henjes-Kunst, F. Palaeomagnetic and Geochronological Study of Late Pan-African and Mesozoic Igneous and Metamorphic Rocks from Central Dronning Maud Land, East Antarctica. *Geol. Jahrb. Reihe B* **2005**, *97*, 7.

61. Sushchevskaya, N.; Belyatsky, B. Geochemical and petrological characteristics of Mesozoic Dykes from Schirmacher Oasis (East Antarctica). In *Dyke Swarms: Keys for Geodynamic Interpretation*; Srivastava, R.K., Ed.; Springer: Berlin/Heidelberg, Germany, 2011; pp. 3–18.

62. Roeser, H.A.; Fritsch, J.; Hinz, K. The Development of the Crust off Dronning Maud Land, East Antarctica. *Geol. Soc.* **1996**, *108*, 243–264. [CrossRef]

63. Reeves, C.; De Wit, M. Making ends meet in Gondwana: Retracing the transforms of the Indian Ocean and reconnecting continental shear zones. *Terra Nova* **2000**, *12*, 272–280. [CrossRef]

64. Jokat, W.; Boebel, T.; König, M.; Meyer, U. Timing and geometry of early Gondwana breakup. *J. Geophys. Res. Solid Earth.* **2003**, *108*, 2428. [CrossRef]

65. Rotstein, Y.; Munschy, M.; Bernard, A. The Kerguelen Province revisited: Additional constraints on the early development of the Southeast Indian Ocean. *Mar. Geophys. Res.* **2001**, *22*, 81–100. [CrossRef]

66. Storey, B.C. The role of mantle plumes in continental breakup: Case histories from Gondwanaland. *Nature* **1995**, *377*, 301–308. [CrossRef]

67. Bialas, R.W.; Buck, W.R.; Studinger, M.; Fitzgerald, P.G. Plateau collapse model for the Transantarctic Mountains–West Antarctic Rift System: Insights from numerical experiments. *Geology* **2007**, *35*, 687–690. [CrossRef]

68. Hinz, K.; Krause, W. The continental margin of Queen Maud Land, Antarctica: Seismic sequences, structural elements and geological development. *Geol. Jahrb. Reihe E* **1982**, *23*, 17–41.

69. Kristoffersen, Y.; Haugland, K. Geophysical evidence for the East Antarctic plate boundary in the Weddell Sea. *Nature* **1986**, *322*, 538. [CrossRef]

70. Kennett, J.P.; Barker, P.F. Latest Cretaceous to Cenozoic climate and oceanographic developments in the Weddell Sea, Antarctica: An ocean-Drilling perspective. *Proc. Ocean Drill. Program Sci. Result* **1990**, *113*, 937–960.

71. O'Connell, S.B. Sedimentary facies and depositional environment of the Lower Cretaceous East Antarctic margin: Sites 692 and 693. *Proc. Ocean Drill. Program Sci. Result* **1990**, *113*, 71–88.

72. Kristoffersen, Y.; Strand, K.; Vorren, T.; Harwood, D.; Webb, P. Pilot shallow drilling on the continental shelf, Dronning Maud Land, Antarctica. *Antarct. Sci.* **2000**, *12*, 463–470. [CrossRef]

73. Emmel, B.; Jacobs, J.; Crowhurst, P.; Austegard, A.; Schwarz-Schampera, U. Apatite single-grain (U-Th)/He data from Heimefrontfjella, East Antarctica: Indications for differential exhumation related to glacial loading? *Tectonics* **2008**, *27*, 13. [CrossRef]

74. Gleadow, A.J.; Duddy, I.R. A natural long-term track annealing experiment for apatite. *Nucl. Tracks* **1981**, *5*, 169–174. [CrossRef]

75. Farley, K.A.; Stockli, D.F. (U-Th)/He Dating of Phosphates: Apatite, Monazite, and Xenotime. *Rev. Mineral. Geochem.* **2002**, *48*, 559–577. [CrossRef]

76. Reiners, P.W.; Farley, K.A.; Hickes, H.J. He diffusion and (U–Th)/He thermochronometry of zircon: Initial results from Fish Canyon Tuff and Gold Butte. *Tectonophysics* **2002**, *349*, 297–308. [CrossRef]

77. Shuster, D.L.; Flowers, R.M.; Farley, K.A. The influence of natural radiation damage on helium diffusion kinetics in apatite. *Earth Planet. Sci. Lett.* **2006**, *249*, 148–161. [CrossRef]

78. Guenthner, W.R.; Reiners, P.W.; Ketcham, R.A.; Nasdala, L.; Giester, G. Helium diffusion in natural zircon: Radiation damage, anisotropy, and the interpretation of zircon (U-Th)/He thermochronology. *Am. J. Sci.* **2013**, *313*, 145–198. [CrossRef]

79. Gleadow, A.J. Fission-track dating methods: What are the real alternatives? *Nucl. Tracks* **1981**, *5*, 3–14. [CrossRef]

80. Dumitru, T.A. A new computer-automated microscope stage system for fission-track analysis. *Nucl. Tracks Radiat. Meas.* **1993**, *21*, 575–580. [CrossRef]

81. Dunkl, I. Trackkey: A Windows program for calculation and graphical presentation of fission track data. *Comput. Geosci.* **2002**, *28*, 3–12. [CrossRef]

82. Hurford, A.J.; Green, P.F. The zeta age calibration of fission-track dating. *Chem. Geol.* **1983**, *41*, 285–317. [CrossRef]

83. Donelick, R.A.; O'Sullivan, P.B.; Ketcham, R.A. Apatite Fission-Track Analysis. *Rev. Mineral. Geochem.* **2005**, *58*, 49–94. [CrossRef]

84. Farley, K.A.; Wolf, R.A.; Silver, L.T. The effects of long alpha-stopping distances on (U-Th)/He ages. *Geochim. Cosmochim. Acta* **1996**, *60*, 4223–4229. [CrossRef]

85. Hourigan, J.K.; Reiners, P.W.; Brandon, M.T. U-Th zonation-dependent alpha-ejection in (U-Th)/He chronometry. *Geochim. Cosmochim. Acta* **2005**, *69*, 3349–3365. [CrossRef]

86. Grubbs, F.E. Sample criteria for testing outlying observations. *Ann. Math. Stat.* **1950**, *21*, 27–58. [CrossRef]

87. Grubbs, F.E. Procedures for detecting outlying observations in samples. *Technometrics* **1969**, *11*, 1–21. [CrossRef]

88. Dixon, W.J. Processing Data for Outliers. *Biometrics* **1953**, *9*, 74–89. [CrossRef]

89. Ketcham, R.A. *Hefty, Version 1.9.1*; Apatite to Zircon, Inc.: Moscow, ID, USA, 2016.

90. Ketcham, R.A.; Carter, A.; Donelick, R.A.; Barbarand, J.; Hurford, A.J. Improved modeling of fission-track annealing in apatite. *Am. Mineral.* **2007**, *92*, 799–810. [CrossRef]

91. Ketcham, R.A.; Carter, A.; Donelick, R.A.; Barbarand, J.; Hurford, A.J. Improved measurement of fission-track annealing in apatite using *c*-axis projection. *Am. Mineral.* **2007**, *92*, 789–798. [CrossRef]

92. Flowers, R.M.; Ketcham, R.A.; Shuster, D.L.; Farley, K.A. Apatite (U–Th)/He thermochronometry using a radiation damage accumulation and annealing model. *Geochim. Cosmochim. Acta* **2009**, *73*, 2347–2365. [CrossRef]

93. Hendriks, B.W.; Engvik, A.K.; Elvevold, S. $^{40}Ar/^{39}Ar$ record of late Pan–African exhumation of a granulite facies terrain, central Dronning Maud Land, East Antarctica. *Mineral. Petrol.* **2013**, *107*, 665–677. [CrossRef]

94. Catuneanu, O.; Wopfner, H.; Eriksson, P.G.; Cairncross, B.; Rubidge, B.S.; Smith, R.M.; Hancox, P.J. The Karoo basins of south-central Africa. *J. Afr. Earth Sci.* **2005**, *43*, 211–253. [CrossRef]

95. Isbell, J.L.; Cole, D.I.; Catuneanu, O. Carboniferous-Permian glaciation in the main Karoo Basin, South Africa: Stratigraphy, depositional controls, and glacial dynamics. In *Resolving the Late Paleozoic Ice Age in Time and Space*; Geological Society of America: Boulder, CO, USA, 2008; pp. 71–82.

96. Wilson, K.M.; Pollard, D.; Hay, W.W.; Thompson, S.L.; Wold, C.N. General circulation model simulations of Triassic climates: Preliminary results. In *Pangea: Paleoclimate, Tectonics, and Sedimentation during Accretion, Zenith, and Breakup of a Supercontinent*; Geological Society of America: Boulder, CO, USA, 1994; Volume 288, pp. 91–116.

97. Carlson, W.D.; Donelick, R.A.; Ketcham, R.A. Variability of apatite fission-track annealing kinetics: I. Experimental results. *Am. Mineral.* **1999**, *84*, 1213–1223. [CrossRef]

98. Galbraith, R.F. *Statistics for Fission Track Analysis*; CRC Press: Boca Raton, FL, USA, 2005.

99. Farley, K.A. Helium diffusion from apatite: General behavior as illustrated by Durango fluorapatite. *J. Geophys. Res. Solid Earth.* **2000**, *105*, 2903–2914. [CrossRef]

100. Reiners, P.W.; Farley, K.A. Influence of crystal size on apatite (U–Th)/He thermochronology: An example from the Bighorn Mountains, Wyoming. *Earth Planet. Sci. Lett.* **2001**, *188*, 413–420. [CrossRef]

101. Flowers, R.M.; Kelley, S.A. Interpreting data dispersion and "inverted" dates in apatite (U–Th)/He and fission-track datasets: An example from the US midcontinent. *Geochim. Cosmochim. Acta* **2011**, *75*, 5169–5186. [CrossRef]

102. Phillips, J.D. Erosion, isostatic response, and the missing peneplains. *Geomorphology* **2002**, *45*, 225–241. [CrossRef]

103. Fernandes, P.; Cogné, N.; Chew, D.M.; Rodrigues, B.; Jorge, R.C.; Marques, J.; Jamal, D.; Vasconcelos, L. The thermal history of the Karoo Moatize-Minjova Basin, Tete Province, Mozambique: An integrated vitrinite reflectance and apatite fission track thermochronology study. *J. Afr. Earth Sci.* **2015**, *112*, 55–72. [CrossRef]

104. Pereira, Z.; Fernandes, P.; Lopes, G.; Marques, J.; Vasconcelos, L. The Permian–Triassic transition in the Moatize–Minjova Basin, Karoo Supergroup, Mozambique: A palynological perspective. *Rev. Palaeobot. Palynol.* **2016**, *226*, 1–19. [CrossRef]

105. Bicca, M.M.; Philipp, R.P.; Jelinek, A.R.; Ketzer, J.M.; dos Santos Scherer, C.M.; Jamal, D.L.; dos Reis, A.D. Permian-Early Triassic tectonics and stratigraphy of the Karoo Supergroup in northwestern Mozambique. *J. Afr. Earth Sci.* **2017**, *130*, 8–27. [CrossRef]

106. Gallagher, K.; Brown, R. Denudation and uplift at passive margins: The record on the Atlantic Margin of southern Africa. *Philos. Trans. R. Soc. Lond. A* **1999**, *357*, 835–859. [CrossRef]

107. Barrett, P. Antarctic Climate history over the Last 100 Million Years. *Terra Antart. Rep.* **1999**, *3*, 53–72.

108. Poole, I.; Cantrill, D.; Utescher, T. A multi-proxy approach to determine Antarctic terrestrial palaeoclimate during the Late Cretaceous and Early Tertiary. *Palaeogeogr. Palaeoclimatol. Palaeoecol.* **2005**, *222*, 95–121. [CrossRef]

109. Thorn, V.C.; DeConto, R. Antarctic climate at the Eocene/Oligocene boundary—Climate model sensitivity to high latitude vegetation type and comparisons with the palaeobotanical record. *Palaeogeogr. Palaeoclimatol. Palaeoecol.* **2006**, *231*, 134–157. [CrossRef]

110. Jenkyns, H.C.; Schouten-Huibers, L.; Schouten, S.; Sinninghe Damsté, J.S. Warm Middle Jurassic–Early Cretaceous high-latitude sea-surface temperatures from the Southern Ocean. *Clim. Past* **2012**, *8*, 215–226. [CrossRef]

111. Lisker, F.; Läufer, A.L. The Mesozoic Victoria Basin: Vanished link between Antarctica and Australia. *Geology* **2013**, *41*, 1043–1046. [CrossRef]

112. Krohne, N.; Lisker, F.; Kleinschmidt, G.; Klügel, A.; Läufer, A.; Estrada, S.; Spiegel, C. The Shackleton Range (East Antarctica): An alien block at the rim of Gondwana? *Geol. Mag.* **2018**, *155*, 841–864. [CrossRef]

113. DeConto, R.M.; Pollard, D. Rapid Cenozoic glaciation of Antarctica induced by declining atmospheric CO_2. *Nature* **2003**, *421*, 245–249. [CrossRef] [PubMed]

114. Ingólfsson, O. Quaternary glacial and climate history of Antarctica. *Dev. Quat. Sci.* **2004**, *2*, 3–43.

115. Jamieson, S.S.; Sugden, D.E. Landscape evolution of Antarctica. In *Antarctica: A Keystone in a Changing World*; National Academies Press: Washington, DC, USA, 2008; pp. 39–54.

116. Yumoto, M.; Ogata, T.; Matsuoka, N.; Matsumoto, E. Riverbank freeze-thaw erosion along a small mountain stream, Nikko volcanic area, central Japan. *Permafr. Periglac. Process.* **2006**, *17*, 325–339. [CrossRef]

117. Studinger, M.; Bell, R.E.; Buck, W.R.; Karner, G.D.; Blankenship, D.D. Sub-ice geology inland of the Transantarctic Mountains in light of new aerogeophysical data. *Earth Planet. Sci. Lett.* **2004**, *220*, 391–408. [CrossRef]

118. Studinger, M.; Bell, R.E.; Fitzgerald, P.G.; Buck, W.R. Crustal architecture of the Transantarctic Mountains between the Scott and Reedy Glacier region and South Pole from aerogeophysical data. *Earth Planet. Sci. Lett.* **2006**, *250*, 182–199. [CrossRef]

119. Elliot, D. The Geological and Tectonic Evolution of the Transantarctic Mountains: A Review. *Geol. Soc.* **2013**, *381*, 7–35. [CrossRef]